

MASTER THESIS

Air flow in a high-traffic urban street canyon: An experimental study investigating turbulent transport in the Landshuter Allee in Munich, Germany.



Figure 1.: Streetview of the environmental monitoring station in the Landshuter Allee street canyon.

SOPHIE ARZBERGER

SUPERVISORS

Prof. Dr. Christoph Thomas

Dr. Wolfgang Babel

Bayreuth, 4.4.2022

Abstract

The contribution of outdoor air pollution to premature mortality could potentially double by 2050. The main reasons for this are the rapid growth of the urban population and the rising urban air pollution. To counteract this development, a new technical approach has been proposed to improve urban air quality: the installation of active cleaning systems (ACS) that are designed to remove nitrogen dioxide (NO_2) and particulate matter (PM) from the outdoor air. This M.Sc. thesis is a part of the REINELUFFT? research project that aims to investigate the cleaning effect of ACS in the Landshuter Allee street canyon in Munich. The efficiency of the ACS is largely controlled by the surrounding air transport and the flow regime of the street. The thesis poses the first step towards gaining a general understanding of the air flow and turbulence regime in the street canyon using the eddy covariance (EC) measurement technique. The main objective was to determine the turbulence characteristics of the Landshuter Allee, with a particular focus on the turbulence generating mechanisms and turbulence strength and how this depends on the canyon-specific flow regimes and the influence of moving vehicles. During the two-month observational period summer '21, the wind was mostly channeled in the Landshuter Allee street canyon. For synoptic flow perpendicular to the street orientation, the wind was partially washed down on the building fronts and reflected back into the street. Overall, the turbulence strength was strongly correlated with the mean wind speed and depended on the flow regime. In general, stronger turbulence was caused by stronger winds and the recirculation flow regime. The shear production of turbulence was additionally influenced by moving vehicles, depending on the traffic intensity. For very weak winds, the generation of turbulence was buoyancy-driven.

Zusammenfassung

Die Anzahl an Menschen, die jährlich vorzeitig an den Krankheitsfolgen von verschmutzter Außenluft sterben, soll sich bis 2050 verdoppeln. Zu den Hauptgründen zählen das schnelle Wachstum der Stadtbevölkerung und die zunehmende Luftverschmutzung in den Städten. Um dem entgegenzuwirken, sollen aktive Luftreinigungssysteme zur Entfernung von Stickstoffdioxid und Feinstaub in besonders belasteten Straßenzügen installiert werden. Der Wirkungsgrad der Luftreinigungssysteme wird maßgeblich vom atmosphärischen Transport im umgebenden Straßenzug beeinflusst. Diese Masterarbeit ist ein Teil des Forschungsprojektes REINELUFT?, das in der Landshuter Allee in München aktive Luftreinigungssysteme aufstellt und deren Reinigungswirkung untersucht. Mithilfe von Eddy-Koviaranz-Turbulenzmessungen wird allgemeines Verständnis des Turbulenzregimes im Straßenzug erlangt werden. Das Hauptziel war es, die Strömungs- und Turbulenzcharakteristiken der Landshuter Allee zu bestimmen, mit besonderem Fokus auf den Mechanismen die Turbulenz erzeugen und der Stärke der Turbulenz in Abhängigkeit von der vorherrschenden Windrichtung und dem Einfluss von Fahrzeugen. Während des zweimonatigen Messzeitraums im Sommer '21 wurde der Wind im Straßenzug größtenteils kanalisiert. Für synoptischen Wind orthogonal zur Orientierung der Straße, bildete sich zum Teil ein Umkehrwirbel. Insgesamt ist die Stärke der Turbulenz in der Landshuter Allee von der Windgeschwindigkeit und dem Strömungsregime abhängig. Höhere Windgeschwindigkeiten und die Ausbildung des Umkehrwirbels führen zu stärkerer Turbulenz. Die Windscherung wird, in Abhängigkeit der Verkehrsintensität, zusätzlich durch die fahrzeuginduzierte Turbulenz (VIT). Bei sehr schwachen Winden wird die Turbulenz hauptsächlich vom Auftrieb bestimmt.

Contents

Abstract	I
Zusammenfassung	III
1. Introduction	1
1.1. Motivation	1
1.2. State of the art: air flow in an urban street canyon	3
1.2.1. How can the air flow in a street canyon be characterized?	3
1.2.2. What role does the vehicle-induced turbulence play?	5
1.3. Research questions	7
2. Methods	9
2.1. Study site	9
2.2. Experimental setup and data acquisition at the LÜB-station	10
2.3. Measurement technique and data processing	13
2.3.1. Theoretical framework: the eddy-covariance method	13
2.3.2. Data corrections and quality assessment	15
2.3.3. Turbulent kinetic energy as a measure for the turbulence strength	19
2.3.4. Determination of atmospheric stability	21
2.4. Meteorological comparative data	22
2.5. Traffic measurements	23
3. Results and discussion	25
3.1. Characteristics of the flow and turbulence regime in the Landshuter Allee street canyon	25
3.1.1. Flow regime: wind direction and wind speed	25
3.1.2. Comparison with synoptic winds over Munich	29
3.1.3. Atmospheric stratification	31
3.1.4. Turbulent kinetic energy	34
3.1.5. Contributions to the TKE tendency	38
3.2. Comparison of street-typical north wind period and west wind dominated period	41
3.3. Influence of traffic on the turbulence regime	46
3.3.1. Traffic in the Landshuter Allee	46
3.3.2. Turbulence characteristics	48
4. Conclusions	57
Acknowledgements	59
Literature	61

Appendices	65
A. Power- and co-spectra (Sonic 2)	65

List of Figures

1.	Streetview of the environmental monitoring station in the Landshuter Allee street canyon.	1
2.	Time series of the NO ₂ concentration, measured at the environmental monitoring station in the Landshuter Allee, over a time period of ten years based on monthly means (blue), 12-month running mean (red) and the tendency (black). The EU limit value of 40 μg/m ³ is indicated as a green line (modified from Bayerisches Landesamt für Umwelt, 2021).	2
3.	Typical flow patterns and vortex regimes for idealized and symmetrical urban street canyons for a perpendicular approach flow and depending on the aspect ratio b/h . Most cities are built with street canyons with an aspect ratio $b/h < 1.5$	3
4.	Driving vehicles influence the turbulence regime in a street canyon both through mechanical and thermal mechanisms. This effect on the turbulence production is referred to as vehicle-induced turbulence (VIT)	5
5.	Location of the (c) measurement site (LÜB-station) on the western side and in the southern section of the (b) Landshuter Allee street canyon (©Bayerisches Landesamt für Umwelt, 2019) (a) in the west of the city of Munich (Map data ©Google Earth, 2022). The tunnelled section of the Landshuter Allee is indicated in blue.	9
6.	Schematic cross section of the Landshuter Allee street canyon with the LÜB-station at the western side of the street.	10
7.	Set up of the instruments on the LÜB-Station. One sonic anemometer was installed at a height of approximately 5 m above ground and extends 1.4 m onto the sidewalk (c). The mini weather station is located at the southwestern corner, approximately 1.73 m above the roof top and 4.73 m above the ground (c). The second sonic anemometer was installed at the southeastern corner of LÜB-Station approximately 2 m above the roof and 5 m above the ground (b).	11
8.	Mean power-spectra (S_{xx}) for the variable x where x is the horizontal or vertical wind velocity or the sonic temperature T_S . The power-spectra were multiplied by the frequency f and normalized by the variance of x . The black solid lines indicates the -2/3 slope that is expected for the inertial subrange in the surface layer. The dashed vertical line corresponds to $\tau = 30$ min and the dotted vertical line to $\tau = 240$ min. The mean power-spectra was computed for the two-month observational period for the measurements of the sidewalk sonic anemometer and further subdivided by daytime (12:00-16:00) and nighttime (00:00 - 4:00). The mean power-spectra for the streetside sonic anemometer are provided in the appendix A.	17

9.	Mean co-spectra ($C_{\sigma_x, w}$ between the vertical wind w and the variable x where x is the horizontal wind or the sonic temperature T_S . The co-spectra were multiplied by the frequency f and normalized by the covariance. The black solid lines indicates the $-4/3$ slope that is expected for the inertial subrange in the surface layer. The dashed vertical line corresponds to $\tau = 30$ min and the dotted vertical line to $\tau = 240$ min. The mean co-spectra was computed for the two-month observational period for the measurements of the sidewalk sonic anemometer and further subdivided by daytime (12:00-16:00) and nighttime (00:00 - 4:00). The mean co-spectra for the streetside sonic are provided in the appendix A.	18
10.	Location of the branch office of the DWD in the Helene-Weber Allee (left, map data ©Google Earth, 2022). The measurement instruments (right, © Deutscher Wetterdienst) are about 1.5 km distant from the LÜB-station.	23
11.	Wind rose plot showing the mean wind speed distribution per 15° wind sector for the half-hourly intervals of the two-month observational period for the sidewalk sonic anemometer (left panel) and the streetside sonic anemometer (right panel).	26
12.	Ensemble average diel of the wind speed (left panel) and the wind direction (right panel) for the half-hourly intervals of the two-month observational period for both sonic anemometers. The respective standard error for the wind speed averages is visualized as shaded area.	27
13.	Diurnal course of the wind direction as percentage per wind sector for each half-hourly interval, averaged over the two-month observational period and as a mean for both sonic anemometers. The colors indicate the five predefined wind sectors "north", "northwest", "east", "south", "west".	27
14.	Percentage per wind sector as daily mean for both sonic anemometers for the two-month observational period. The colors indicate the five predefined wind sectors "north", "northwest", "east", "south", "west".	28
15.	Box plot of the wind speed for the sidewalk sonic (top panel) and the streetside sonic (bottom panel) divided by 10° wind direction sectors for the two-month observational period. The colors indicate the five predefined wind sectors "north", "northwest", "east", "south", "west". Boxplots are a standardized way of showing the distribution of quantitative data. The position and length of the box is determined by the upper and lower quartile. The line inside the box indicates the median. The whiskers extend 1.5 times the interquartile range (difference between the upper and the lower quartile) from the center of the box. All data points beyond the end of the whiskers are plotted individually as outliers.	28
16.	Wind rose plot illustrating the mean wind speed distribution per 15° wind sector at the DWD-operated meteorological station in the Helene-Weber Allee for the hourly observations during the two-month measurement period.	29
17.	Comparison of the measured wind direction during the two-month observational period for the LÜB-station in the Landshuter Allee and DWD-operated meteorological station in the Heinrich-Weber Allee. Each data point represents an hourly interval. The colors indicate the five predefined wind sectors "north", "northwest", "east", "south", "west".	30
18.	Presumed flow pattern in the Landshuter Allee street canyon when the synoptic easterly winds are reflected by the building fronts and reversed to westerly winds.	30

19. Visualization of the atmospheric stratification in the Landshuter Allee during the two-month observational period. Top: Daily percentage of half-hourly intervals of neutral (orange), stable (purple) and unstable (cyan) atmospheric stratification for the sidewalk sonic anemometer (left) and the streetside sonic anemometer (right). Bottom: Number of data points per stability class for both sonic anemometers. Each data point represents one half-hourly interval. The stability classes of stable and unstable atmospheric stratification are further subdivided according to the size of the value of ζ (Table 4). The total number of intervals per sonic anemometer and stability range is written above the respective bar. The time of the day is represented by the transparency in both plots. High transparency illustrates nighttime and low transparency depicts daytime. 33
20. Violin plot to illustrate the distribution of the Monin-Obukhov stability parameter ζ per flow regime and per sonic anemometer. The dotted lines correspond to $\zeta = -0.0625$ and $\zeta = 0.0625$ and mark the transition from unstable ($\zeta < -0.0625$) to neutral ($-0.0625 < \zeta < 0.0625$) to stable conditions ($\zeta > 0.0625$). The colors indicate the five wind direction sectors: "north" ($350^\circ - 30^\circ$), "northwest" ($300^\circ - 350^\circ$), "east" ($30^\circ - 120^\circ$), "south" ($120^\circ - 250^\circ$), "west" ($250^\circ - 300^\circ$). Compared to a box plot, the violin plot shows the full distribution of the data. The probability density is visualized on both sides of the boxplot. 34
21. Box plot illustrating the average ensemble diel for the half-hourly intervals of the the two-month measurement period of the TKE for the streetside sonic anemometer (blue) and the sidewalk sonic anemometer (red). 35
22. Box plot of the TKE to illustrate the daily average for the street-side sonic (blue) and the sidewalk sonic (red) for the two-month observational period. 36
23. Daily percentage of westerly and northwesterly wind as a function of the daily mean TKE differentiated by sonic anemometer. Each data point represents one half-hourly interval of the two-month observational period. The solid lines correspond to the respective regression line with R^2 as coefficient of determination. . . . 36
24. Dependency of TKE on the wind direction. Left panel: Wind rose plot illustrating the mean TKE per 15° wind sector differentiated by sonic anemometer. Right panel: Box plot showing the average TKE per predefined wind sector. The wind sectors "north" ($350^\circ - 30^\circ$), "northwest" ($300^\circ - 350^\circ$), "east" ($30^\circ - 120^\circ$), "south" ($120^\circ - 250^\circ$) and "west" ($250^\circ - 300^\circ$) are differentiated by color. 37
25. TKE as a function of the mean wind speed \bar{u} . Each data point represents one half-hourly interval of the two-month observational period. The flow regimes are differentiated by color and the solid lines correspond to the respective regression line with R^2 as coefficient of determination. 37
26. Boxplot illustrating the ensemble averaged diel for the half-hourly intervals of the the two-month measurement period for the buoyancy production (yellow) and shear generation term (cyan) in the TKE budget equation for the sidewalk sonic anemometer (left panel) and the streetside sonic anemometer (right panel). . . . 38
27. Wind rose plots for the two-month observational period illustrating the mean buoyancy flux H (left panel) and the mean friction velocity u_* (right panel) per 15° wind sector differentiated by sonic anemometers. The five wind sectors "north", "northwest", "east", "south" and "west" are highlighted by color. 39

28.	Percentage per wind sector as daily mean for both sonic anemometers. The five predefined wind sectors "north", "northwest", "east", "south" and "west" are differentiated by color. The two 48h time periods that represent the site-typical north wind (20. and 21.7.) and west wind dominated conditions (7. and 8.9.) are framed by red boxes.	41
29.	Time series plot of the hourly mean wind speed and wind direction for the two 48 h time periods that represent site-typical north wind (20. and 21.7.) and west wind dominated conditions (7. and 8.9.). The wind speed is displayed as solid (20. and 21.7.) and dashed line (7. and 8.9.). The wind direction is represented by single points - crosses (20. and 21.7.) and diamonds (7. and 8.9.) - and further differentiated by color. The colors indicate the five predefined wind sectors "north" (350°- 30°), "northwest" (300°- 350°), "east" (30°- 120°), "south" (120°- 250°), "west" (250°- 300°).	42
30.	Time series plot of the hourly mean solar radiation SR (green), the sonic temperature T_S (purple) and the buoyancy flux H (orange) for the two 48 h time periods that represent site-typical north wind (20. and 21.7.) and west wind dominated conditions (7. and 8.9.). H is scaled by a factor of three. The north wind period is displayed as solid line and the west wind period as dashed line.	43
31.	Time series plot of hourly mean of the buoyancy (orange) and the shear (green) contribution to the TKE budget equation and the total TKE (purple) for the two 48h time periods that represent site-typical north wind (20. and 21.7.) and west wind dominated conditions (7. and 8.9.). The north wind period is displayed as solid line and the west wind period as dashed line.	44
32.	Ensemble average diel of the traffic volume (orange) on the two driving lanes directly adjacent to the LÜB-station station and the associated mean driving speed (cyan) for the two-month time period from the 16.07.2021 to the 15.09.2021 divided by day of the week. The dotted line shows the ensemble average for the weekend (Saturday and Sunday) and the solid line the average for the weekdays (Monday through Friday).	46
33.	Distribution of the vehicle types for the two south-orientated driving lanes closest to the LÜB-station station over the course of the two-month observational period. Left panel: Diurnal ensemble average of the percentage (lines) and the total number (bars) of truck-like vehicles per hourly interval differentiated by weekday (cyan) and weekend (orange). Right panel: Distribution of the vehicle count per day in the week in the two main categories "truck-like" (darkgrey) and "car-like" (lightgrey). Each day occurred equally often during the measurement period.	47
34.	Ensemble average diel of the TKE for the given half-hour intervals over the two-month observational period. Depicted is the average per measuring system (sidewalk and streetside sonic) with further subdivision by the day of the week (weekdays and weekend).	49
35.	Boxplot illustrating the overall ratio of the shear to the buoyancy term in the TKE budget equation depending on the measuring sonic anemometer (left) and depending on the day of the week (right).	50
36.	Boxplot illustrating the ensemble average diel of the hourly shear to buoyancy ratio as an average for both sonic anemometers. The ratio of the terms in the TKE budget equation was further subdivided by weekday (cyan) and weekend (orange). Unity is indicated as solid line.	50

-
37. TKE as a function of the number of vehicles per 30 min interval (left) and as a function of the mean driving speed per 30 min interval (right). The data intervals for the two-month measurement period are categorized by the time of the day: 5:00-8:30 (purple squares), 9:00-13:30 (red circles), 14:00-19:30 (orange triangles) and 20:00-4:30 (yellow diamonds). Dynamic bin averages are illustrated in black and the error bars denote \pm one standard deviation. 52
38. Time series of the TKE for the time period from 00:00 to 4:00 for the night between the 20.07. and the 21.7. The temporal resolution is 1.5 s. The red lines indicate the mean TKE over the 4-hour period $\pm 5\sigma$ 53
39. Box plots illustrating the average wind speed \bar{u} for the two-month measurement period differentiated by weekend and weekday for the LÜB-station in the Landshuter Allee (left panel) and the DWD station in the Helene-Weber Allee (right panel). 54
40. Dependency of the friction velocity u_* on the mean wind speed \bar{u} differentiated by weekend and weekday. The mean values of u_* correspond to dynamic bin values of \bar{u} . Each data point represents one half-hourly interval of the two-month measurement period. The error bars denote \pm one standard deviation. 55
41. Mean power-spectra (S_{xx}) for the variable x where x is the horizontal or vertical wind velocity or the sonic temperature T_S . The power-spectra were multiplied by the frequency f and normalized by the variance of x . The black solid lines indicates the $-2/3$ slope that is expected for the inertial subrange in the surface layer. The dashed vertical line corresponds to $\tau = 30$ min and the dotted vertical line to $\tau = 240$ min. The mean power-spectra was computed for the two-month observational period for the measurements of the streetside sonic anemometer and further subdivided by daytime (12:00-16:00) and nighttime (00:00 - 4:00). . . . 65
42. Mean co-spectra ($C_{o_x, w}$) between the vertical wind w and the variable x where x is the horizontal wind or the sonic temperature T_S . The co-spectra were multiplied by the frequency f and normalized by the covariance. The black solid lines indicates the $-4/3$ slope that is expected for the inertial subrange in the surface layer. The dashed vertical line corresponds to $\tau = 30$ min and the dotted vertical line to $\tau = 240$ min. The mean co-spectra was computed for the two-month observational period for the measurements of the streetside sonic anemometer and further subdivided by daytime (12:00-16:00) and nighttime (00:00 - 4:00). 66

List of Tables

2.	List of parameters measured by the ClimaVUE50 mini weather station	12
3.	List of parameters measured by both uSonic-3-Cage MP ultrasonic anemometers	12
4.	Determination of the stratification of the surface layer depending on the Monin-Obukhov stability parameter ζ (Table adapted from Foken, 2017).	22
5.	Overview of the average vehicle count per day per category for the two-month measurement period. Only the two south-oriented driving lanes closest to the LÜB-station were considered.	24
6.	Subdivision of the wind directions into five defined wind sectors	25
7.	Overview of the total number of half-hourly intervals and the corresponding percentage of the respective stability regime depending on the sonic anemometer and the time of the day.	31
8.	Overview of the mean TKE (m^2s^{-2}) over the entire two-month observational period, separated by the sonic anemometer, the day of the week and only the daytime.	48
9.	Overview of the hourly number of truck-like vehicles in the time period from 00:00 to 4:00 for the night between the 20.07. and the 21.7., the hourly number of all vehicles, the corresponding percentage of truck-like vehicles per hour and the number of spikes detected in the TKE signal of the streetside sonic. All data points outside the range of the mean TKE $\pm 5\sigma$ were considered as spikes. . . .	54

List of abbreviations and symbols

Abbreviation	Description
ABL	atmospheric boundary layer
ACS	air cleaning system
a.s.l.	above sea level
EU	European Union
LES	large eddy simulation
LÜB	Lufthygienische Landesüberwachungssystem Bayern
PM	particulate matter
RANS	Reynolds-averaged Navier-Stokes equations
REINELUFFT?	RE inigen NE ue LUF tFiltersysTeme von urbanem Stickstoffdioxid?
RSL	roughness sublayer
TKE	turbulent kinetic energy
VIT	vehicle-induced turbulence
UHI	urban heat island
WHO	World Health Organization

Symbol	Description	Unit
b	street canyon width	m
c_p	specific heat at constant pressure	$\text{Jkg}^{-1}\text{K}^{-1}$
\bar{e}	turbulent kinetic energy	m^2s^{-2}
f	frequency	Hz
f_c	coriolis frequency	s^{-1}
g	gravitational acceleration	ms^{-2}
H	buoyancy flux	Wm^{-2}
h	street canyon height	m
K_m	turbulent diffusion coefficient of momentum	Wm^{-2}
L	Obukov-length	m
NO_2	nitrogen dioxide	μgm^{-3}
p	air pressure	hPa
Q_E	sensible heat flux	Wm^{-2}
Q_H	latent heat flux	Wm^{-2}
RH	relative humidity	%
SR	solar radiation	Wm^{-2}
T	air temperature	K
T_S	sonic temperature	K
t	time	s
u_*	friction velocity	ms^{-1}
\bar{u}	mean wind velocity	ms^{-1}
u	along-wind component	ms^{-1}

Symbol	Description	Unit
v, w	cross-wind component after coordinate rotation	ms^{-1}
x, y	horizontal direction	m
z	height above ground level	m
α	ratio of the exchange coefficients	
ϵ	energy dissipation	m^2s^{-3}
ζ	Monin-Obukov stability parameter	
ϕ_m	universal function	
θ_v	virtual potential temperature	K
κ	von Karman constant	
λ	adiabatic lapse rate	Kkm^{-1}
ρ	air mass density	kgm^{-3}
ϕ	wind direction	$^\circ$

1. Introduction

1.1 Motivation

Air pollution is considered to be one of the world's largest environmental health threats (Lelieveld et al., 2015). According to the World Health Organization (WHO) the effects of outdoor air pollution led to 4.2 million premature deaths worldwide and more than half a million in the European Union (EU) in 2016 (Sicard et al., 2021). Due to the rapid growth of the urban population and the rising urban air pollution, the contribution of outdoor air pollution to premature mortality could potentially double by 2050 (Lelieveld et al., 2015). To protect human health, the EU passed the ambient air quality directive (European Council Directive 2008/50/EC) to set legally binding limits for the concentrations of major air pollutants such as particulate matter (PM₁₀ and PM_{2.5}) and nitrogen dioxide (NO₂) in outdoor air. However, the current levels of air pollutants in cities continue to exceed the EU standards (Sicard et al., 2021).

A new technical approach to improve urban air quality and to help to adhere to the legally binding thresholds is the installation of active cleaning systems (ACS) that are designed to remove NO₂ and PM from the air. The research project REINELUFFT? (**RE**Inigen **NE**ue **LUF**tFiltersysTeme von urbanem Stickstoffdioxid?) aims at determining if ACS can help to reduce the concentration of NO₂ in the surroundings of an urban street canyon with intense traffic. To formulate specific use recommendations, the first independent comprehensible scientific evaluation of the efficiency of ACS will be performed with three-year funding from the Bavarian State Agency for Environment and Consumer Protection. The question of where and under which conditions what level of reduction in air pollutants can be expected from the installation of ACS is decisive for economic and environmental policy-making concerning their utilization.

The study is conducted in the Landshuter Allee street canyon in the center of the city of Munich. Due to its high importance for the traffic circulation in Munich, the four-lane street canyon is known for its high traffic intensity and high concentration of air pollutants. To

monitor the development of the concentration of air pollutants in the Landshuter Allee, the Bavarian Environmental Agency is operating an environmental monitoring station in the southern section of the street canyon. The development of the NO₂-concentration over the last decade showed a downward trend in the Landshuter Allee, but the street canyon continues to exceed the EU-wide target value (Figure 2). According to the Federal Environmental Agency (Umweltbundesamt, UBA), the annual mean NO₂ concentration of 54 µg/m³ in the Landshuter Allee in 2020 was nationwide the highest and well above the EU limit value of 40 µg/m³. It was considerably higher than the second largest annual mean NO₂ concentration of 47 µg/m³ that was measured in the Schlosstraße in Ludwigsburg and strongly exceeded the overall mean value of 29 µg/m³ for all monitoring stations nationwide located in a traffic-influenced urban environment (Umweltbundesamt, 2021). Therefore, the Landshuter Allee street canyon is the most suitable choice for conducting this research, both because of its critical role in the discussion about urban air pollution and the pre-existing scientific infrastructure.

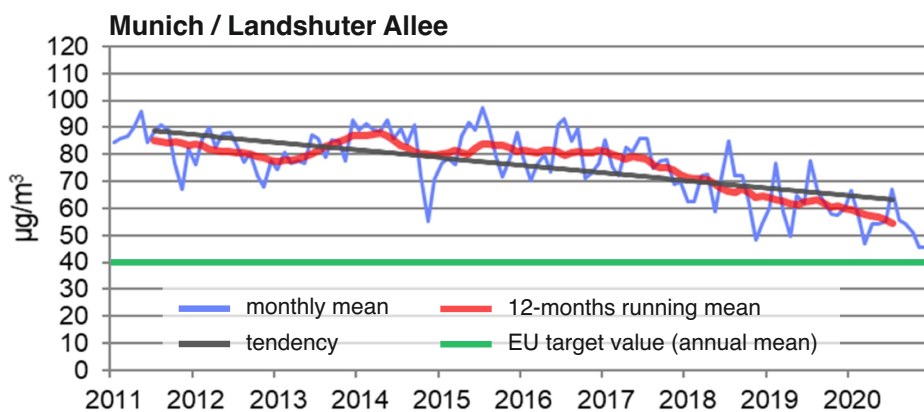


Figure 2.: Time series of the NO₂ concentration, measured at the environmental monitoring station in the Landshuter Allee, over a time period of ten years based on monthly means (blue), 12-month running mean (red) and the tendency (black). The EU limit value of 40 µg/m³ is indicated as a green line (modified from Bayerisches Landesamt für Umwelt, 2021).

The research project REINELUFFT? is subdivided into four subprojects that are led by the University of Bayreuth (air flow and chemistry), the University of Augsburg (measuring network), the Technical University of Munich (traffic) and the Regensburg University of Applied Sciences (adsorption and catalysis). The subproject at the University of Bayreuth will quantify how ACS are influenced by the chemical composition of the air as well as the atmospheric transport within the ACS and its surroundings. To this end,

the air transport and quality will be analyzed in laboratory and field experiments and additionally modeled using large eddy simulations (LES). How this master thesis aims to contribute to the project and what research questions ought to be answered is described in more detail in chapter 1.3.

1.2 State of the art: air flow in an urban street canyon

1.2.1 How can the air flow in a street canyon be characterized?

One major factor that influences the effectiveness of an ACS is the volume of air that flows through the system. This volume mainly depends on the the air transport surrounding the ACS and the flow regime of the street. The airflow in street canyons is highly site-dependent because the morphology of building canopies differs greatly (Zajic et al., 2011). Street canyons are defined as streets that are flanked by buildings on both sides to create a canyon-like environment (Karra et al., 2017). The aspect ratio is commonly used to geometrically characterize a street canyon. It is defined as the ratio of the canyon width b to the canyon height h .

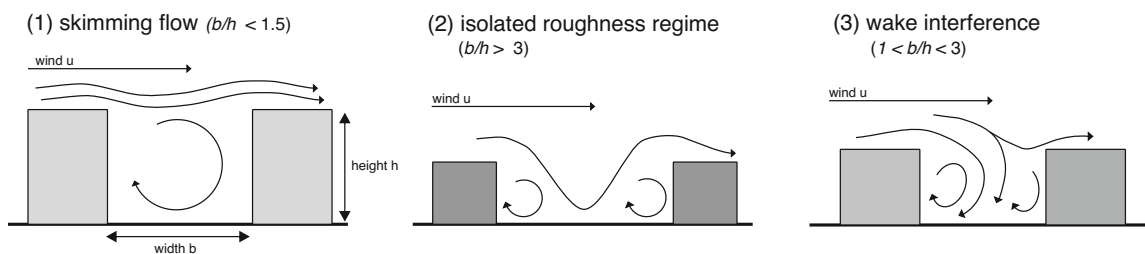


Figure 3.: Typical flow patterns and vortex regimes for idealized and symmetrical urban street canyons for a perpendicular approach flow and depending on the aspect ratio b/h . Most cities are built with street canyons with an aspect ratio $b/h < 1.5$.

Besides the morphology, the flow patterns within the building canopy are also influenced by the direction and wind speed of the approach flow (Zajic et al., 2011). If the wind is perpendicular to the street orientation, three idealized flow regimes can be differentiated depending on the aspect ratio (Figure 3). 1) For an aspect ratio of $b/h > 3$ there is only little interaction between the individual building wakes. 2) If the street canyon has an aspect ratio of $b/h < 1.5$, the air skims over the buildings and a stable vortex develops in the canyon. 3) Between these two regimes, for an aspect ratio $1.5 < b/h < 3$ there

is interference between the individual building wakes (Zajic et al., 2011). In contrast, an approach flow aligned with the canyon orientation causes wind canalization and an increase in wind speed (Yousefian et al., 2021). However, the flow regime of a heterogeneous street canyon, as it is typically found in city environments, can significantly differ from the flow in an idealized symmetrical street canyon.

Under these urban cross-flow scenarios, dominated by buildings wakes and channeling effects, turbulent exchange processes become the controlling factor of street ventilation and pollution dispersion (Klein and Galvez, 2015). Turbulence is commonly generated in two primary ways: wind-shear induced and thermally induced (Foken, 2017). In urban environments, The turbulence production by shear is mainly controlled by the high surface roughness of urban structures and the approach flow. The wake diffusion behind bluff roughness elements and the formation of drag causes strong turbulence as well as efficient vertical and horizontal mixing and potentially results in stationary vortices that can lead to significant dispersive fluxes (Roth, 2000).

As a result of an increased frictional drag on the mean flow over built-up urban terrain, wind speeds in cities are reduced compared to rural areas. These low wind speeds only have the potential to produce little turbulence and thermal effects come into play (Roth, 2000). Because of thermal convection due to the anthropogenic heat flux and the increased heat capacity of building and street surfaces, urban areas are commonly significantly warmer than rural areas. This effect is referred to as urban heat island (UHI). The temperature gradient between a city and its surroundings is especially strong during nighttime under cloudless and weak-wind conditions (Sarrat et al., 2006).

An additional influencing factor on the turbulence regime is the stratification of the atmospheric boundary layer (ABL). The stratification of the ABL is connected to the stability of the atmosphere which describes the tendency of air to move in a vertical direction due to the temperature and density structure of the atmosphere. In a stably stratified atmosphere, the air flow is only intermittently turbulent and vertical motion is suppressed. In contrast, under unstable conditions, vertical motion is enhanced and the flow is turbulent. Neutral air has no tendency to change but the turbulence is potentially very strong (Foken, 2017). Stable stratification suppresses vertical turbulent mixing and can therefore lead to an accumulation of pollutants in the air (Li et al., 2016). The nocturnal ABL is in

general stably stratified. However, due to the UHI, stable stratification occurs much less in urban areas compared to its rural surroundings (Li et al., 2016).

1.2.2 What role does the vehicle-induced turbulence play?

The large-scale transport of air pollutants is mainly governed by the atmospheric mean flow. During the transport, the airborne material undergoes several physical processes, including turbulent mixing, and chemical transformations until it is diluted or deposited. The local-spread of air pollutants is largely influenced by small-scale atmospheric processes. Strong turbulent mixing leads to a rapid dispersion and dilution of pollutants. In contrast, weak turbulence and low wind speeds often result in an accumulation of pollutants which leads to episodes of high air pollution in urban environments. In these cases, when very little turbulence is produced by wind or thermal mechanisms, moving vehicles potentially reduce the concentration of pollutants in the air through turbulence, either mechanically induced by the vehicle wake or thermally induced by the hot exhaust gas (Cai et al., 2020; Di Sabatino et al., 2003) (Figure 4). Especially on the very localized scale of a street canyon, vehicles can significantly impact the vertical distribution of freshly emitted pollutants (Makar et al., 2021). To be able to understand the transport and dispersion of pollutants in a street canyon, it is hence necessary to investigate the role of vehicle-induced turbulence (VIT).



Figure 4.: Driving vehicles influence the turbulence regime in a street canyon both through mechanical and thermal mechanisms. This effect on the turbulence production is referred to as vehicle-induced turbulence (VIT)

VIT has already been investigated for various configurations and urban structures, including wind tunnel installations (Kastner-Klein et al., 2001; Ahmad et al., 2005), field experiments (Alonso-Estébanez et al., 2012; Kalthoff et al., 2005) and modelling approaches (Cai et al., 2020; Di Sabatino et al., 2003; Makar et al., 2021). In these studies it was demonstrated that a significant impact on the air flow due to vehicle movement can be expected and that there are several factors that influence the turbulence production and dissipation by vehicles in a street canyon. One is the vehicle size. Due to the higher drag, the amount of turbulence produced by large vehicles, like busses or trucks, is larger compared to standard passenger cars with a more streamline shape (Alonso-Estébanez et al., 2012, Cai et al., 2020). The modelling based study by Cai et al. (2020) quantified this effect: the turbulent kinetic energy (TKE) induced by a moving truck was approximately 1.6 times larger than that of a sport utility vehicle (SUV) and about 2.5 times larger than that of a car. Another factor is the driving speed. In general, with increasing driving speed more turbulence is produced (Alonso-Estébanez et al., 2012). The field-study by Alonso-Estebanez et. al. (2012) showed a significant linear correlation between the TKE and vehicle speed with a regression slope of 0.27 ($R^2 = 0.75$) for trucks. However, the TKE did not exhibit a functional relationship with vehicle speed for the passenger cars (Alonso-Estébanez et al., 2012). Additionally, there is a strong correlation between traffic intensity and VIT. In a field experiment Vachon et al. (2002) showed that up to a threshold range of 350 to 400 vehicles per hour and driving lane, the turbulence production increases relative to the number of vehicles per hour. Beyond this threshold, the distance between the vehicles decreases and so does the driving speed. This leads to a comparatively lower turbulence production during high traffic conditions (Vachon et al., 2002). Stationary vehicles, i.e. parking vehicles at the roadside or in a traffic jam, create a blocking effect and can significantly influence the surrounding air flow (Cai et al., 2020). The direction of the approaching flow also influences the VIT. If the wind direction is opposite to the vehicle movement, the contribution is the highest. Wind that aligns with the driving direction leads to a comparatively small contribution to the turbulence production (Cai et al., 2020).

1.3 Research questions

The B.Sc. thesis by Sophia Ramer, as a contribution to the REINELUFFT? project, provides a thorough analysis of the flow regimes in the Landshuter Allee street canyon, depending on the large-scale weather conditions and the correlation of the NO₂ concentration with the prevailing wind speed and direction under consideration of seasonality. Ramer's work showed that the wind in the Landshuter Allee is mostly channeled, independent of the synoptic forcing. However, for specific large-scale weather conditions and synoptic flow perpendicular to the street orientation, the flow direction is deflected by the building fronts and reversed in the street canyon. Ramer's B.Sc. thesis also showed that wind speed and wind direction have a significant influence on the NO₂ concentrations. Higher wind speeds lead to lower concentrations of NO₂ and so do wind directions that differ from the channeled north wind.

This M.Sc. thesis is a follow-up to Ramer's B.Sc. thesis and poses the first step towards gaining a general understanding of the turbulence regime in the Landshuter Allee street canyon. The analysis is guided by the following research questions:

1. How do the turbulence generating mechanisms and the strength of turbulence in the Landshuter Alle depend on the canyon-specific flow regimes?
2. What is the effect of vehicle-induced turbulence on the TKE?

On the basis of the current state of knowledge, it is hypothesized that

- (i) air flow in a street canyon is greatly influenced by its morphology and the presence of flow-disturbing obstacles. The turbulent flow within the urban canopy is coupled to the synoptic boundary layer flow and can consequently be characterized as a function of the wind direction.
- (ii) the turbulence strength is connected to the wind speed. In weak wind conditions, the vertical turbulent mixing is significantly suppressed.
- (iii) there is a distinct difference in the diurnal cycle of the turbulence intensity and the turbulent flow characteristics depending on the traffic intensity. The shear production is intensified by driving vehicles and especially in high traffic situations with slow-moving traffic, the buoyancy force is enhanced by the hot exhaust gas.

2. Methods

2.1 Study site

The Landshuter Allee street canyon was chosen as the study site for the research project because it is nationwide the street where the highest concentrations of air pollutants are measured. To monitor the development of the concentration of air pollutants, the Bavarian Environmental Agency is operating an environmental monitoring station (LÜB-station) in the southern section and on the western side of the street ($48^{\circ} 9' 58.38''$ N $11^{\circ} 32' 11.508''$ E, 520 m a.s.l.). The LÜB-station (Figure 5) provides the required infrastructure for the field experiments of the project.



Figure 5.: Location of the (c) measurement site (LÜB-station) on the western side and in the southern section of the (b) Landshuter Allee street canyon (© Bayerisches Landesamt für Umwelt, 2019) (a) in the west of the city of Munich (Map data © Google Earth, 2022). The tunnelled section of the Landshuter Allee is indicated in blue.

The Landshuter Allee is a north-south oriented street canyon with a total length of 4.5 km, featuring many exit and entrance ramps. The four middle traffic lanes are tunnelled for

2. Methods

approximately 430 m (Figure 5). Due to the many traffic lanes - four in each driving direction - the Landshuter Allee has a large width of 54 m. The buildings flanking the Landshuter Allee are about 20 m high on both sides (Figure 6). This results in a large aspect ratio $b/h \approx 2.7$. The Landshuter Allee is additionally characterized by a high abundance of urban trees, both at the western roadside and as a separator between the traffic lanes.

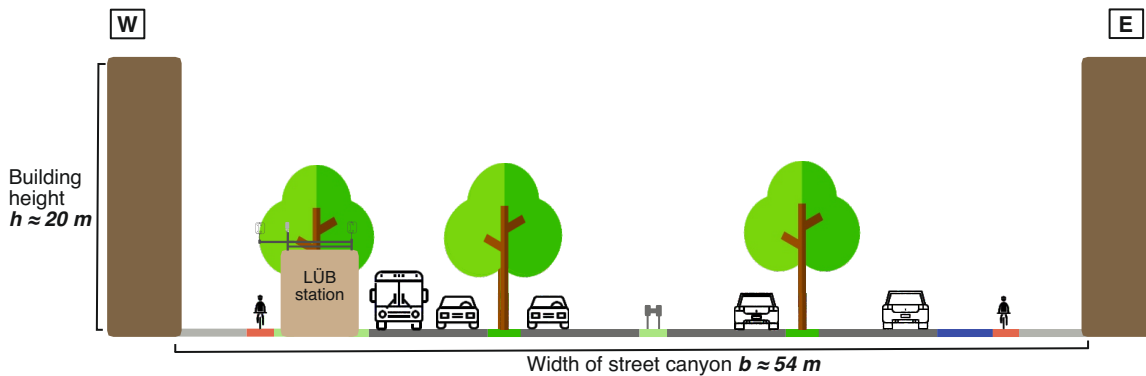


Figure 6.: Schematic cross section of the Landshuter Allee street canyon with the LÜB-station at the western side of the street.

2.2 Experimental setup and data acquisition at the LÜB-station

To analyze the turbulence characteristics and the flow regime of the Landshuter Allee, two three-dimensional ultrasonic anemometer (uSonic-3-Cage MP, Metek GmbH), to resolve and quantify the turbulence, and one mini weather station (ClimaVUE50, Campbell Scientific Inc.) were set up on the roof of LÜB-Station at a height of approximately 5 m. One sonic anemometer was mounted on a 1.5 m long crossbar on the western side of the roof, above the sidewalk and one was installed on the eastern side of the roof, facing the street (Figure 7). The intention of this setup was to analyze both the direct effect of the vehicles on the turbulence characteristics at the roadside as well as the air flow surrounding the pedestrians on the sidewalk.

The sonic anemometer on the pedestrian side of the LÜB-Station was installed on the 21.05.2021 along with the mini weather station. The sonic anemometer on the street-side was set up about two months later, on the 15.07.2021. Both sonic anemometers

were aligned with the main wind direction north in an azimuth angle of 0° . Since their installation, both sonic anemometers have been continuously recording data. For the subsequent analysis of the flow and turbulence characteristics, a two-month time period from the 16.07.2021 to the 15.09.2021 is taken into account.

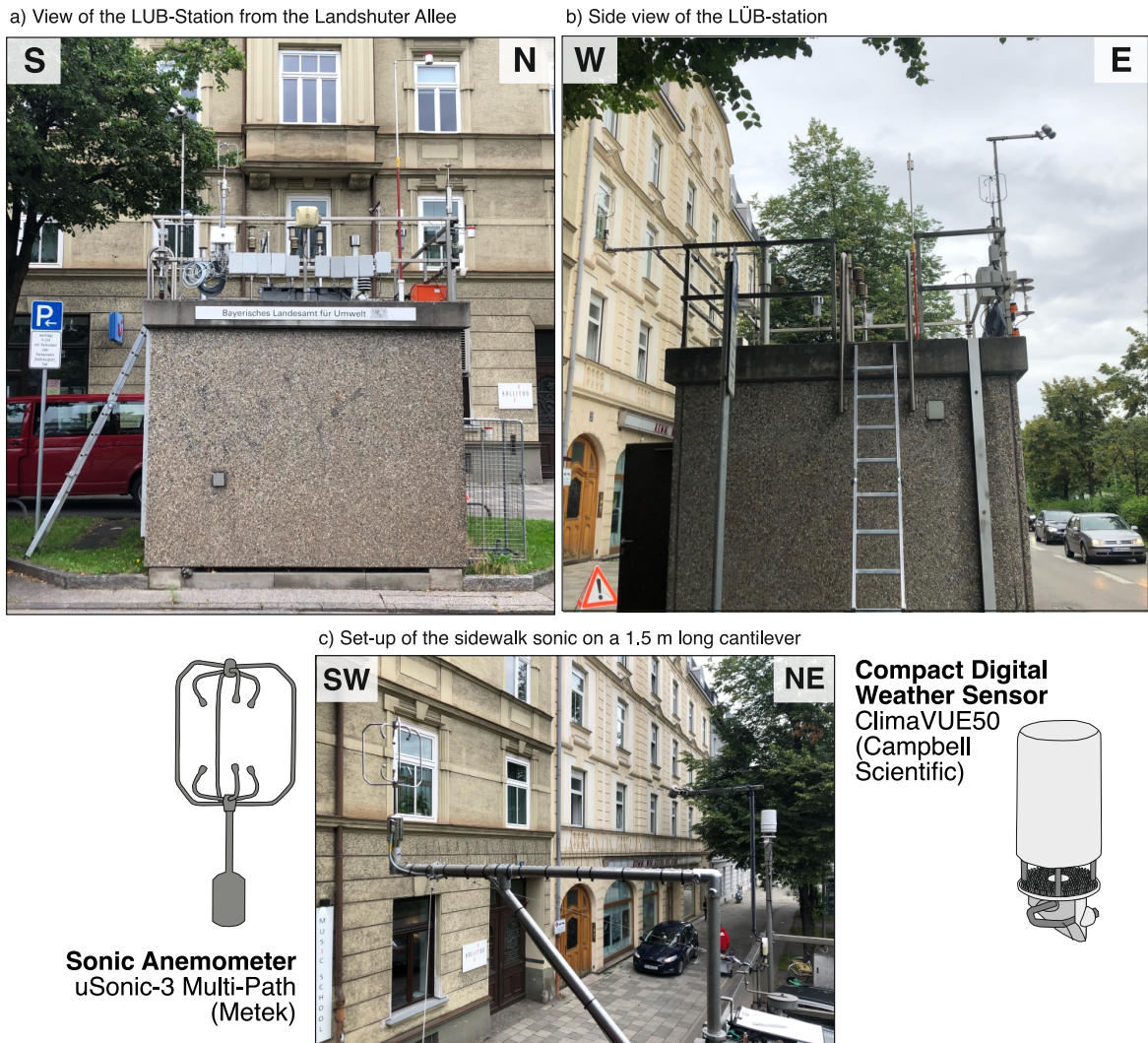


Figure 7.: Set up of the instruments on the LÜB-Station. One sonic anemometer was installed at a height of approximately 5 m above ground and extends 1.4 m onto the sidewalk (c). The mini weather station is located at the southwestern corner, approximately 1.73 m above the roof top and 4.73 m above the ground (c). The second sonic anemometer was installed at the southeastern corner of LÜB-Station approximately 2 m above the roof and 5 m above the ground (b).

The sonic anemometers reported data at a high frequency of 20 Hz. The acquired data was recorded on a data logger (Model CR6, Campbell Sci. Inc.) at the sampling frequency and written to hourly files. The mini weather station has a sampling rate of

2. Methods

10 s. This data was summarized as statistics of 1 minute and 10 minutes and written to daily files. Both hourly and daily files were sent to a Raspberry Pi, transmitted to a university-operated cloud application and additionally saved on an internal Micro-SD card. The measured parameters are listed in Table 1 for the mini weather station and in Table 2 for the sonic anemometers.

Table 2.: List of parameters measured by the ClimaVUE50 mini weather station

Parameter	Unit
air temperature T	$^{\circ}\text{C}$
solar radiation SR	Wm^{-2}
relative humidity RH	%
precipitation	mm
wind speed \bar{u}	ms^{-1}
wind direction ϕ	$^{\circ}$

Table 3.: List of parameters measured by both uSonic-3-Cage MP ultrasonic anemometers

Parameter	Unit
sonic temperature T_S	$^{\circ}\text{C}$
optimized wind components u,v,w	ms^{-1}
vector and scalar averages of wind velocity \bar{u}	ms^{-1}
and wind direction ϕ	$^{\circ}$
inclinometer (pitch, roll and azimuth)	$^{\circ}$

The high frequent three dimensional wind measurements obtained by the sonic anemometers are the integral component of the eddy covariance (EC) method. The raw data was processed with the MATLAB-based Bmmflux software that was written for the analysis of EC-measurements (Thomas et al., 2009). The main processing steps are described in more detail in chapter 2.3.2. For further computations and statistical analysis the open source software R (Version 3.6.1) with the development environment RStudio (Version 1.2.5042) was used (R Core Team, 2021).

In the analysis of the turbulence characteristics, the data was often examined for the diurnal cycle and the differences between daytime and nighttime conditions. Over the course of the two-month measurement period, dawn in the Landshuter Allee occurred between 5:00 and 6:30 and the sunrise between 5:30 and 6:50. The sunset was between 19:20 and 21:10 and dusk between 20:00 and 22:00. If necessary, the data was split by a dynamic indicator for the time of the day that is output directly from the Bmmflux software.

2.3 Measurement technique and data processing

2.3.1 Theoretical framework: the eddy-covariance method

The EC-technique is the most commonly applied method to investigate turbulent fluxes in the atmospheric surface layer. The direct measurement method is based on high frequent measurements of the horizontal and vertical components of wind speed and other scalar parameters. The high sampling rate ensures that the full frequency range of the present eddy structures can be captured (Foken, 2017).

The EC-method is mathematically based on the Reynolds-averaged Navier-Stokes- equations (RANS). The Navier-Stokes equations are partial differential equations that express the conservation of mass, momentum and energy of viscous fluids and describe their motion. They can be expressed as

$$\frac{\delta u}{\delta t} = -u \frac{\delta u}{\delta x} - v \frac{\delta u}{\delta y} + w \frac{\delta u}{\delta z} + \nabla^2 u - \frac{1}{\rho} \frac{\delta p}{\delta x} + f \cdot v \quad (2.3.1)$$

$$\frac{\delta v}{\delta t} = -u \frac{\delta v}{\delta x} - v \frac{\delta v}{\delta y} + w \frac{\delta v}{\delta z} + \nabla^2 v - \frac{1}{\rho} \frac{\delta p}{\delta y} - f \cdot u \quad (2.3.2)$$

$$\underbrace{\frac{\delta w}{\delta t}}_{\text{Tendency}} = \underbrace{-u \frac{\delta w}{\delta x} - v \frac{\delta w}{\delta y} + w \frac{\delta w}{\delta z}}_{\text{Advection}} + \underbrace{\nabla^2 w}_{\text{Viscous forces}} + \underbrace{-\frac{1}{\rho} \frac{\delta p}{\delta y}}_{\text{Pressure gradient force}} + \underbrace{-f \cdot u}_{\text{Coriolis force}} + \underbrace{g}_{\text{Gravitational acceleration}} \quad (2.3.3)$$

where u , v and w are the three dimensional wind components, p is the atmospheric pressure, ρ the air density, f the Coriolis parameter and g the gravitational acceleration (Foken, 2017).

To include turbulent motions in the Navier-Stokes equations, all variables need to be decomposed into a mean and a fluctuating part. For the separation of the fluctuating component x' from the mean flow \bar{x} the Reynolds decomposition is applied:

$$x = \bar{x} + x' \quad (2.3.4)$$

where x represents the wind components or a scalar parameter and the overbar symbolizes the time average that determines the range of motions that contribute to the calculated flux. Fluxes are then computed as the average of the instantaneous products of the perturbations. An important step for extracting the turbulence is the suitable choice

of averaging time span to accurately decompose the flow into a mean and a turbulent part (Foken, 2017).

The so-called Reynolds postulates provide averaging rules for the turbulent values x' and y' while a represents a constant:

$$\text{I} \quad \overline{x'} = 0 \quad (2.3.5)$$

$$\text{II} \quad \overline{xy} = \overline{x}\overline{y} + \overline{x'y'} \quad (2.3.6)$$

$$\text{III} \quad \overline{\overline{xy}} = \overline{xy} \quad (2.3.7)$$

$$\text{IV} \quad \overline{ax} = a\overline{x} \quad (2.3.8)$$

$$\text{V} \quad \overline{x + y} = \overline{x} + \overline{y} \quad (2.3.9)$$

After the application of the Reynolds's decomposition and following the Boussinesq-approximation (Boussinesq, 1877), the turbulent equations of motion are already greatly simplified. For the atmospheric boundary layer additional approximations can be made to further simplify the turbulent equations. Firstly, horizontal homogeneity ($\delta/\delta x = 0$; $\delta/\delta y = 0$) and stationarity ($\delta/\delta t = 0$) are assumed. As a consequence, micrometeorological measurements are only valid under steady state conditions and require a mostly homogeneous surface. Secondly, the flow is presumed to be incompressible ($\frac{\delta \overline{u}}{\delta x} = 0$; $\frac{\delta \overline{w}}{\delta z} = 0$; $\overline{w} = 0$). Close to the surface, the effect of the Coriolis force and the pressure gradient force can be neglected in the flux gradient relationship. Additionally, the surface layer is assumed to be divergence free ($\frac{\delta \overline{u'w'}}{\delta z} \approx 0$) resulting in height-constant covariances. Following these approximations and according to the second Reynold's postulate, the total flux is equal to the covariance:

$$u^* = \overline{-u'w'}; \quad \frac{Q_H}{\rho c_p} = \overline{T'w'}; \quad \frac{Q_E}{\rho \lambda} = \overline{q'w'} \quad (2.3.10)$$

This poses the requirement and the basis for the direct measurement principle of the EC-technique (Foken, 2017).

2.3.2 Data corrections and quality assessment

The EC-method requires flux measurements over a flat and horizontally homogeneous surface under stationary conditions. These requirements can rarely be fully met, especially not in urban environments. Unlike for mostly homogeneous natural vegetation, EC-measurements in highly heterogeneous urban landscapes are directly affected by several small-scale processes, i.e. traffic and manufacturing where the spatial and temporal changes are associated with human activities. Therefore, EC-measurements in urban environments require additional care in data filtering and need to be interpreted with caution (Järvi et al., 2018). The post-processing of the raw EC-data is required to not only correct for instrumental limitations but also to make sure that the assumptions for applying the EC-method are fulfilled. The post-processing of the EC-data, including the corrections and the computation of the covariances and several other parameters, was done with the MATLAB-based Bmmflux software. Firstly, the raw data is filtered by instrumental flags and the application of physically meaningful plausibility limits. Outliers in the high frequent time series are detected and removed using a despiking routine (Vickers and Mahrt, 1997). A cross-correlation analysis is performed to shift all measurements to the same time base.

In order to fulfill the requirement of a negligible mean vertical wind component, the horizontal axis needs to be rotated into the mean wind direction. However, forcing the main vertical wind speed to zero caused implausible rotation angles in the post-processing of the EC-data in this analysis. This tilt error can lead to a cross-contamination between the flux components and a subsequent falsification of the computed fluxes. Therefore, a 2-D tilt correction was applied that did not let the mean vertical wind speed vanish. Not forcing the vertical wind speed to zero potentially allows a significant mean vertical wind speed which can directly reflect on the buoyancy effects.

2.3.2.1 Frequency-response correction

Systematic errors due to the physical limitations of the sensors and the data analysis technique have to be considered in the turbulence analysis. The EC-technique provides accurate turbulence measurements but it remains frequency band-limited. This leads to a loss of data in both the low and the high frequency range of the signal and a subsequent underestimation of the turbulent fluxes. The magnitude of this underestimation needs

to be quantified to be accounted for in the analysis. To prevent flux loss at the high frequency and partially the low frequency range a spectral correction method according to Moore (1986) is commonly applied. The magnitude of the correction is usually less than 10 % but can be up to 30 % in extreme atmospheric conditions or if the sensors are not in an optimal position (Moore, 1986). In this analysis, the Moore correction accounted for up to 3 % flux loss for the covariances. For the variances, the magnitude was in the range of 11.5 to 12.5 %.

2.3.2.2 Choice of perturbation time scale τ

The spatial and temporal scale of atmospheric motions are linked (Taylor, 1938). Their relation can be expressed in the spectrum of atmospheric turbulence which describes the energy distribution of eddy structures according to their wavelength. The part of the spectrum that is of interest in micrometeorology describes the exchange of energy and matter between the land, the ocean and the atmosphere. It can be subdivided into three major frequency ranges: The low-frequency range is the energy-containing range. It receives the energy directly from the mean flow and drives the small scale turbulent motions. At intermediate frequencies in the inertial subrange, the energy of the eddy structures decreases by successively breaking down in size. According to Kolmogorov's local similarity theorem, the turbulence becomes locally isotropic and homogeneous while the eddy structures at large scale are non isotropic. In the high-frequency range of the micro-scale spectrum the energy is dissipated through viscosity (Foken, 2017). According to Kolmogorov's hypotheses the decay of homogeneous turbulence from low to high frequencies follows a $-2/3$ power-law relationship:

$$f \cdot S_X(f) \approx f^{-2/3}; S_X(f) \approx f^{-5/3} \quad (2.3.11)$$

The corresponding fluxes typically obey a $-4/3$ power-law scaling:

$$f \cdot C_{o_x,w}(f) \approx f^{-4/3}; C_{o_x,w}(f) \approx f^{-7/3} \quad (2.3.12)$$

The turbulent co-spectra and power-spectra are analyzed to determine the most suitable perturbation time scale τ . This is a decisive step for the flux computation in the post-processing of EC-data because low-frequency loss can result from insufficiently long

averaging times and if τ is too short, the low contribution to the fluxes is missed. With an increasing τ , the systematic error can be reduced but this may potentially introduce non-stationarity. In the past several decades, time periods between 10 and 60 minutes for τ have proven to be most suitable (Järvi et al., 2018). For the spectral analysis in this study, the data was processed twice: for $\tau = 30$ min and $\tau = 240$ min. From this, the mean power-spectra (Figure 8) and co-spectra (Figure 9) were computed.

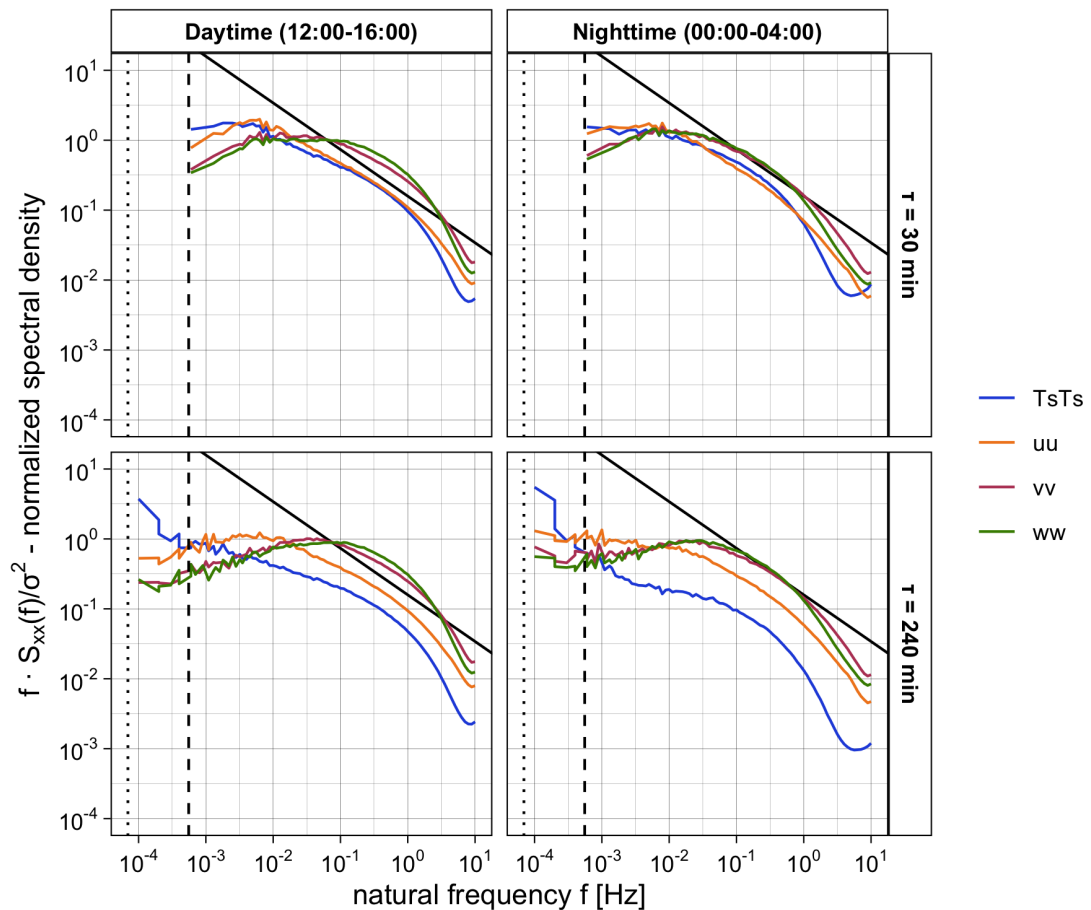


Figure 8.: Mean power-spectra (S_{XX}) for the variable x where x is the horizontal or vertical wind velocity or the sonic temperature T_S . The power-spectra were multiplied by the frequency f and normalized by the variance of x . The black solid lines indicates the $-2/3$ slope that is expected for the inertial subrange in the surface layer. The dashed vertical line corresponds to $\tau = 30$ min and the dotted vertical line to $\tau = 240$ min. The mean power-spectra was computed for the two-month observational period for the measurements of the sidewalk sonic anemometer and further subdivided by daytime (12:00-16:00) and nighttime (00:00 - 4:00). The mean power-spectra for the streetside sonic anemometer are provided in the appendix A.

The decisive features of these plots are the spectral peaks and the slopes. For an averaging time of 30 min and during daytime, the slopes of the power-spectra and co-spectra in the inertial subrange were closer to the expected $-2/3$ and $-4/3$ compared to

2. Methods

the 240 min averaging time and to nighttime. In the high-frequency range, the deviations from the optimized curve can be explained with instrumental limitations. This effect was more pronounced during the night than during the day. In the low-frequency range, the normalized energy density of the T_S power-spectra converged for $\tau = 30$ min and continued to increase for $\tau = 240$ min but did not show a distinct peak. This strong non-stationarity for temperature is typical for the urban surface layer because of the thermal regime and the heating of the urban surfaces.

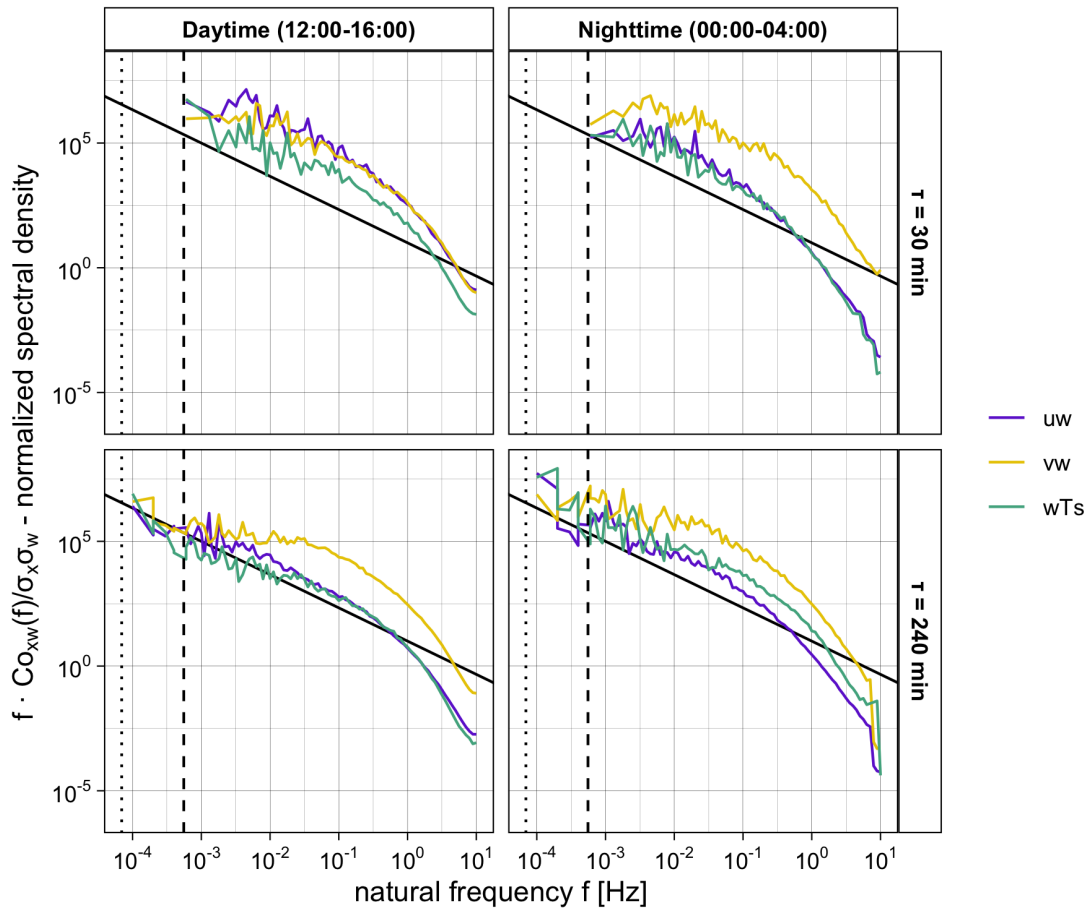


Figure 9.: Mean co-spectra ($C_{o_{x,w}}$ between the vertical wind w and the variable x where x is the horizontal wind or the sonic temperature T_S). The co-spectra were multiplied by the frequency f and normalized by the covariance. The black solid lines indicates the $-4/3$ slope that is expected for the inertial subrange in the surface layer. The dashed vertical line corresponds to $\tau = 30$ min and the dotted vertical line to $\tau = 240$ min. The mean co-spectra was computed for the two-month observational period for the measurements of the sidewalk sonic anemometer and further subdivided by daytime (12:00-16:00) and nighttime (00:00 - 4:00). The mean co-spectra for the streetside sonic are provided in the appendix A.

The peaks in spectral density for the power-spectra for the 30 min averaging time were in the range of 0.001 to 0.1 Hz. From 12:00 to 16:00, the spectral density of S_{uu} and S_{ww}

reached a plateau in the frequency range from 0.01 to 0.1 Hz. For the time span from 00:00 to 4:00, S_{uu} and S_{ww} peaked at a frequency of 0.1 Hz. The co-spectra peaked at approximately 0.01 Hz both at day- and nighttime.

With the calculation $\lambda = \bar{u} / f$, the eddy wavelengths can be determined and a rough approximation of the size of the peak energy containing eddies can be made. For an average horizontal windspeed of 0.60 ms^{-1} for daytime conditions, the eddy size was in the range of several tens of meters during the day and during the night, for an average horizontal windspeed of 0.27 ms^{-1} for nighttime conditions, the eddy size was in the range of a few tens of meters.

Overall, the 30 min averaging time is sufficient to sample any motions that contribute to the transport adequately. Longer perturbation timescales introduce non-stationarity that could lead to a distortion of the computed total covariance. The analysis of the 240 min averaging time showed that for larger τ mesoscale motions are already taken into account.

2.3.3 Turbulent kinetic energy as a measure for the turbulence strength

The turbulent kinetic energy (TKE) is commonly used as a measure of the turbulence strength. It describes the mean kinetic energy per unit mass associated with eddies in turbulent flow and is defined as half the sum of the variances of the velocity fluctuations:

$$TKE = \bar{e} = \frac{1}{2} (\overline{u'^2} + \overline{v'^2} + \overline{w'^2}) = 0.5 \overline{u_i'^2} \quad (2.3.13)$$

TKE can be produced by mechanical shear or buoyancy. It is then transferred down the scales towards smaller length and time scales, and is dissipated by viscous forces at the Kolmogorov scale. The contribution of the various processes is reflected in the TKE tendency equation:

$$\underbrace{\frac{\delta \bar{e}}{\delta t}}_{TKE \text{ tendency}} = - \underbrace{\frac{\bar{w}}{\delta z} \frac{\delta \bar{e}}{\delta z}}_{Advection} - \underbrace{\frac{g}{\theta_v} \overline{w' \theta_v'}}_{Buoyancy} - \underbrace{\frac{\overline{w' u'}}{\delta z} \frac{\delta \bar{u}}{\delta z}}_{Mechanical shear} - \underbrace{\frac{\delta(\overline{w' e})}{\delta z}}_{Turbulent transport} - \underbrace{\frac{1}{\bar{\rho}} \frac{\delta(\overline{w' p'})}{\delta z}}_{Pressure transport} - \underbrace{\epsilon}_{Viscous dissipation} \quad (2.3.14)$$

This equation is obtained by multiplying the Navier-Stokes equation for turbulent flow with u'_i and is commonly used in the evaluation which atmospheric processes contribute to the production or consumption of TKE (Foken, 2017).

2.3.3.1 Contribution of buoyancy and shear τ

The TKE is computed automatically by the Bmmflux-software from the measured velocity fluctuations. To get an insight into the TKE tendency, the buoyancy production term and the shear generation term need to be determined. The contribution of the buoyancy to the TKE budget can be calculated from the direct measurement of the buoyancy flux $\overline{w'\theta'_v}$ and the mean virtual potential temperature $\overline{\theta_v}$.

To determine the shear term, the vertical gradient of the wind speed $\frac{\delta \overline{u}}{\delta z}$ is required. It cannot be obtained from direct measurements but it can be approximated from the measured momentum flux u_* on the basis of the K-approach (Foken, 2017).

$$u_*^2 = K_m \cdot \frac{\delta \overline{u}}{\delta z} \quad (2.3.15)$$

Under non-neutral conditions, the eddy diffusivity of momentum K_m can be expressed as

$$K_m = \frac{\kappa z u_*}{\phi_m(\zeta)} \quad (2.3.16)$$

with the von Karman constant κ , the measuring height z and the universal function ϕ_m :

$$\phi_m(\zeta) = \begin{cases} 0.95(1 - 11.6\zeta) & \zeta < 0 \\ 0.95 + 7.8\zeta & \zeta > 0 \end{cases} \quad (2.3.17)$$

where ζ is the Monin-Obukhov stability parameter (Eq. 2.3.19).

From this, the vertical wind speed gradient can be calculated as:

$$\frac{\delta \overline{u}}{\delta z} = \frac{u_* \phi_m}{\kappa z} \quad (2.3.18)$$

2.3.4 Determination of atmospheric stability

There are two concepts to describe the stability condition of the atmosphere: static and dynamic stability. The concept of static atmospheric stability only considers buoyant effects. It is estimated as an adiabatic process and can be determined by comparing the vertical gradient of the virtual potential temperature with the respective average adiabatic lapse rate γ (Foken, 2017).

The concept of dynamic atmospheric stability also takes shear-generated turbulence into account. Dynamic stability is often assessed on the basis of the Monin-Obukhov- similarity theory. It describes the vertical motion in the atmospheric surface layer as a function of the Monin-Obukhov key parameters: the height above ground z , the normalized surface momentum flux, also referred to as friction velocity u_* and the buoyancy flux $\overline{w'\theta'_v}$ (Foken, 2017).

From this, the dimensionless Monin-Obukhov stability parameter ζ is derived:

$$\zeta = \frac{z}{L} \quad (2.3.19)$$

It is defined by the height z and the Obukov length L :

$$L = -\frac{\overline{\theta}_v u_*^3}{\kappa g (\overline{w'\theta'_v})} \quad (2.3.20)$$

Where κ is the von Karman constant, u_* the friction velocity, $\frac{g}{\overline{\theta}_v}$ the buoyancy parameter and $\overline{w'\theta'_v}$ the buoyancy flux.

The stability parameter ζ is commonly used to describe the atmospheric stratification in the surface layer (Table 4). It describes the relative contribution of buoyancy and shear to the turbulence regime and is typically in the range of -3 to 1. For dynamically unstable conditions ζ is negativ, for dynamically stable conditions positive and it approaches zero for neutral stratification. If ζ is strongly negative, the turbulent flow is buoyancy-dominated and the exchange processes are controlled by free convection. A large, positive value for ζ indicates a strong stable stratification with potential decoupling from the surface (Foken, 2017).

Table 4.: Determination of the stratification of the surface layer depending on the Monin-Obukhov stability parameter ζ (Table adapted from Foken, 2017).

Stratification	Stability Parameter ζ	
unstable	$\zeta < -1$	free convection
	$-0.0625 > \zeta > -1$	dependent on u_*
neutral	$0.0625 > \zeta > -0.0625$	
stable	$1 > \zeta > 0.0625$	dependent on u_*
	$\zeta > 1$	independent from z

To assess the atmospheric stratification from EC-measurements, the Bmmflux-software computes the stability parameter ζ . Only ζ values in the range of -3 and 1 were considered for the analysis of the atmospheric stratification in this thesis.

2.4 Meteorological comparative data

The German weather service (DWD) is operating a meteorological station at its branch office in the Helene-Weber-Allee in Munich. It is located about 1.5 km bee-line north/north-east of the LÜB-station and records various parameters including wind speed and wind direction. The instruments are intentionally installed at a certain distance of potential flow-disturbing obstacles (Figure 10). The measured air flow is therefore less disturbed compared to the flow surrounding the sensors in the Landshuter Allee.

In general, the surface layer of the urban atmosphere can be divided into a deep roughness sublayer (RSL) and the overlying inertial sublayer. Near the top of the urban canopy, an intense shear layer forms, whose turbulence properties differ systematically from the inertial sublayer. The RSL in cities has a substantial depth comparable to forest ecosystems, because of the large building height and is strongly influenced by the individual buildings. The lowest part of the RSL is the canopy layer. Within the canopy layer, the turbulent exchange processes are significantly influenced by the building structures and street morphology. As a consequence, the convective and radiative coupling between the air flow within the canopy, i.e. in a street canyon, and the RSL above the roofs is potentially restricted and the canopy layer may maintain a very locally adapted flow and turbulence regime (Aubinet et al., 2012).

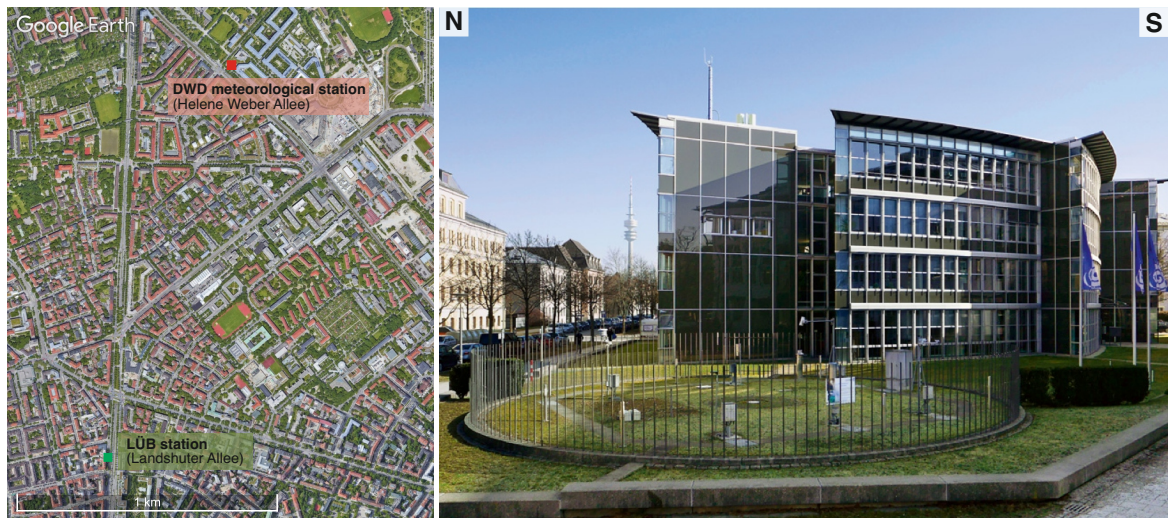


Figure 10.: Location of the branch office of the DWD in the Helene-Weber Allee (left, map data ©Google Earth, 2022). The measurement instruments (right, © Deutscher Wetterdienst) are about 1.5 km distant from the LÜB-station.

Due to its setup, the air flow measured at the DWD station in the Heinrich-Weber-Allee is expected to be more representative for the synoptic deeper boundary flow over Munich compared to the LÜB station in the Landshuter Allee. To compare the air flow at the two stations, the data from the DWD station was downloaded in hourly resolution via the open-access Climate Data Center (CDC) for the required two-month time period.

2.5 Traffic measurements

The Landshuter Allee is an important traffic artery in Munich which is used by many commuters daily to get in and out of the city center. In addition, several bus lines are operating in the Landshuter Allee. At the bus station 30 m north of the LÜB-station, buses run at intervals of up to every 4 min, depending on the time of the day.

To analyze the traffic in the Landshuter Allee, the Kreisverwaltungsrat (KVR) of Munich has installed double induction loops under each driving lane. With this, it is possible to gain insight into the traffic intensity, the driving speed and the distribution of vehicle categories.

For the analysis of the VIT two datasets are used: 15 min aggregates of the traffic volume and the mean driving speed and hourly aggregates for the traffic volume per vehicle category. In the hourly dataset, the vehicles are subdivided into 9 different categories

2. Methods

and further summarized in the two main categories: truck-like vehicles and car-like vehicles (Table 5). From both datasets, the traffic measurements for the two south-oriented driving lanes closest to the LÜB-station were taken into account. The datasets were provided by the REINELUFFT? subproject *Traffic* (Frederik Bachmann, TU Munich, pers. com.) for the predefined two-month time period.

Table 5.: Overview of the average vehicle count per day per category for the two-month measurement period. Only the two south-oriented driving lanes closest to the LÜB-station were considered.

Vehicle category	average vehicle count per day	
Motorcycle	192	car-like 4378 (90.6%)
Car	3764	
Car + trailer	12	
Delivery van	411	
Bus	228	truck-like 452 (9.4%)
Truck	90	
Truck + trailer	32	
Semitrailer	101	
Unclassified	0	

3. Results and discussion

3.1 Characteristics of the flow and turbulence regime in the Landshuter Allee street canyon

The turbulence in the Landshuter Allee was characterized for five flow regimes defined by the wind direction sectors "north", "northwest", "east", "south" and "west" (Table 6). This subdivision is based the findings of the study by Ramer (2021) on the wind regimes of the Landshuter Allee and takes into account the distribution of wind speed and direction as well as the turbulence properties of the Landshuter Allee street canyon.

Table 6.: Subdivision of the wind directions into five defined wind sectors

wind sector	north	northwest	west	south	east
wind direction	350°- 360°, 0°- 30°	300°- 350°	250°- 300°	120°- 250°	30°- 120°

3.1.1 Flow regime: wind direction and wind speed

The air flow in the Landshuter Allee street canyon was dominated by northerly winds during the two-month observational time period (Figure 11). The wind speed was in the range of 0 to 1.6 ms⁻¹ for both sonic anemometers, with a mean wind speed of 0.46 ms⁻¹ for the sonic anemometer over the sidewalk and 0.66 ms⁻¹ for the sonic anemometer on the street side.

The magnitude of the wind speed was dependent on the time of the day (Figure 12, left panel). During the night the wind speed was the lowest. With increasing solar radiation and convection after dawn, the wind speed increased, reached a steady level in the late morning and decreased again in the late afternoon. The wind was generally stronger on the street side with a persistent difference between both sonic anemometers. The measured wind speed on the street side was ≈ 0.2 ms⁻¹ higher during the night and ≈ 0.3 ms⁻¹ higher during the day while the increase in wind speed at dawn as well as

3. Results and discussion

the decrease at nightfall occurred at the same time. The mean wind direction also differed depending on the time of the day (Figure 12, right panel). From approximately 5:00 to 21:00, north was the dominating wind direction for both sonic anemometers. Starting at 21:00, the wind direction shifted from north to east to southeast. The southernmost mean wind direction was observed at 2:00, with 110° for the streetside sonic and 150° for the sidewalk sonic. Afterwards the wind direction shifted back to north.

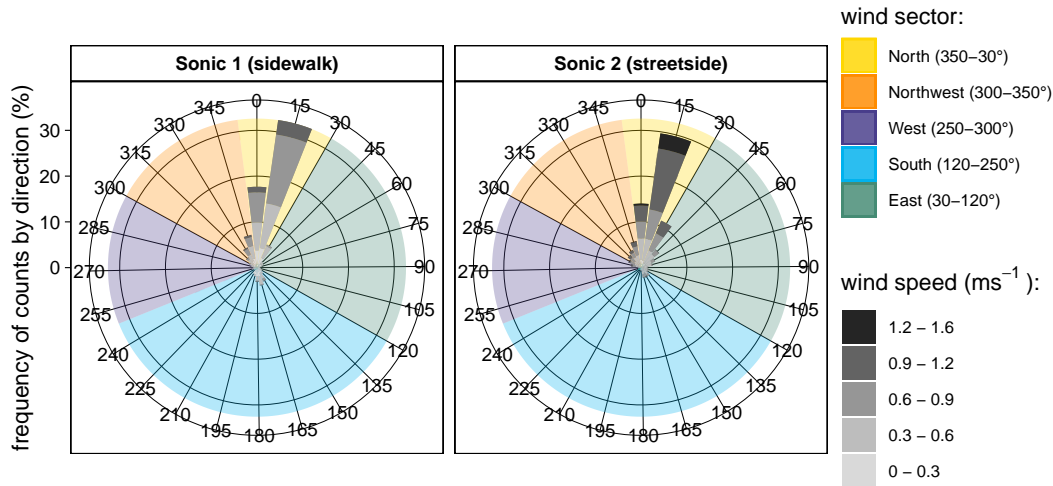


Figure 11.: Wind rose plot showing the mean wind speed distribution per 15° wind sector for the half-hourly intervals of the two-month observational period for the sidewalk sonic anemometer (left panel) and the streetside sonic anemometer (right panel).

The average distribution of the flow regime fluctuated over the course of the day (Figure 13). Northerly winds dominated throughout most of the day, with a maximum proportion of up to 70 % in the early morning hours. The largest percentage of southerly wind was observed during the night, with a contribution in the range of 25 to 40 % from nightfall until dawn. The percentage of easterly winds was highest in the early morning hours (20 %). For the daylight hours, northwest was the most common wind direction after north. The percentage of northwesterly winds started to increase in the late morning, from a consistently low level of 5-10 % during the night, up to 25 % in late afternoon. The percentage of westerly winds was in a consistent range of 1 to 10 % throughout the day. Overall, southerly and easterly winds played a larger role at nighttime and in the early morning hours while northwesterly winds were more often observed at daytime in the afternoon. The daily wind sector distribution fluctuated over the course of the observational period (Figure 14). The first days of the measurement campaign, up until the 20.07.21, were dominated by percentages of north wind of up to 90 %. Overall,

3.1. Characteristics of the flow and turbulence regime in the Landshuter Allee street canyon

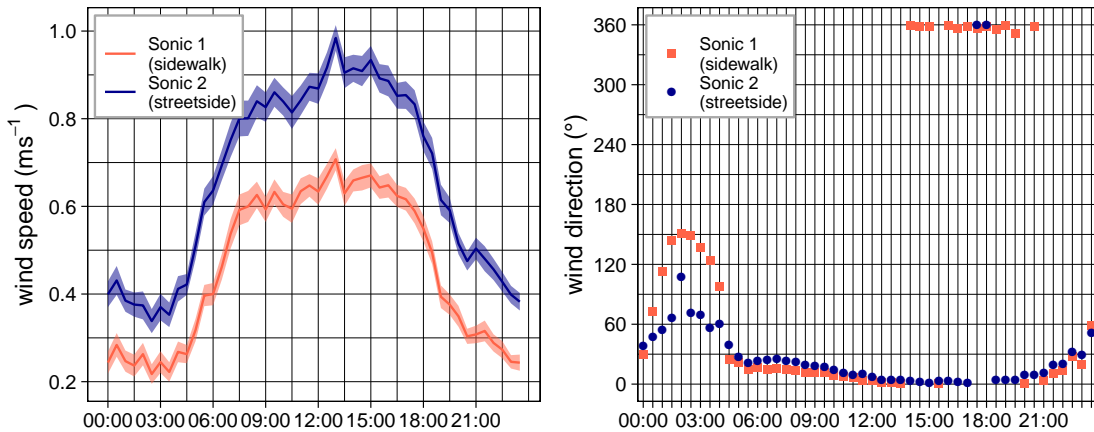


Figure 12.: Ensemble average diel of the wind speed (left panel) and the wind direction (right panel) for the half-hourly intervals of the two-month observational period for both sonic anemometers. The respective standard error for the wind speed averages is visualized as shaded area.

north remained the main wind sector with an average daily contribution of 54 %. The daily percentage of southerly winds was in the range of 1 to 54 % and the contribution of easterly winds was between 1 % and 35 %. There were many days with no or hardly any west wind and individual days, i.e. the 1.09.2021 and the 7.09.21, with a west wind contribution higher than 10 %. The daily percentage of northwesterly wind fluctuated strongly. Several days with high a high contribution of northwesterly winds stand out. During the first week in September and on two days in August, the 23.08.21 and the 24.08.21, the percentage of northwesterly wind was above 50 %.

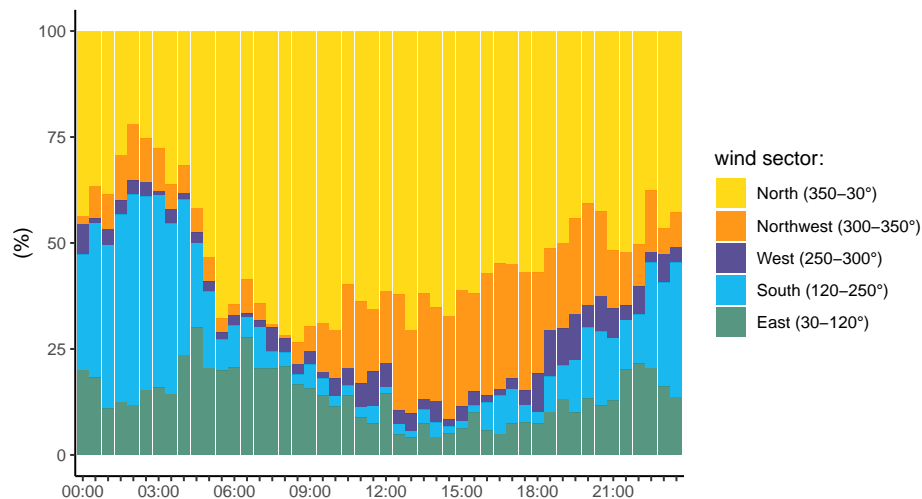


Figure 13.: Diurnal course of the wind direction as percentage per wind sector for each half-hourly interval, averaged over the two-month observational period and as a mean for both sonic anemometers. The colors indicate the five predefined wind sectors "north", "northwest", "east", "south", "west".

3. Results and discussion

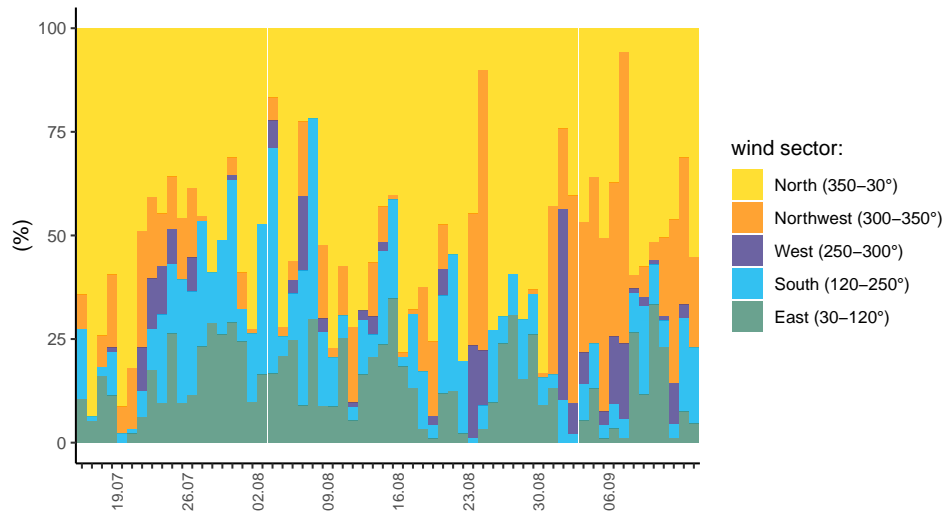


Figure 14.: Percentage per wind sector as daily mean for both sonic anemometers for the two-month observational period. The colors indicate the five predefined wind sectors "north", "northwest", "east", "south", "west".

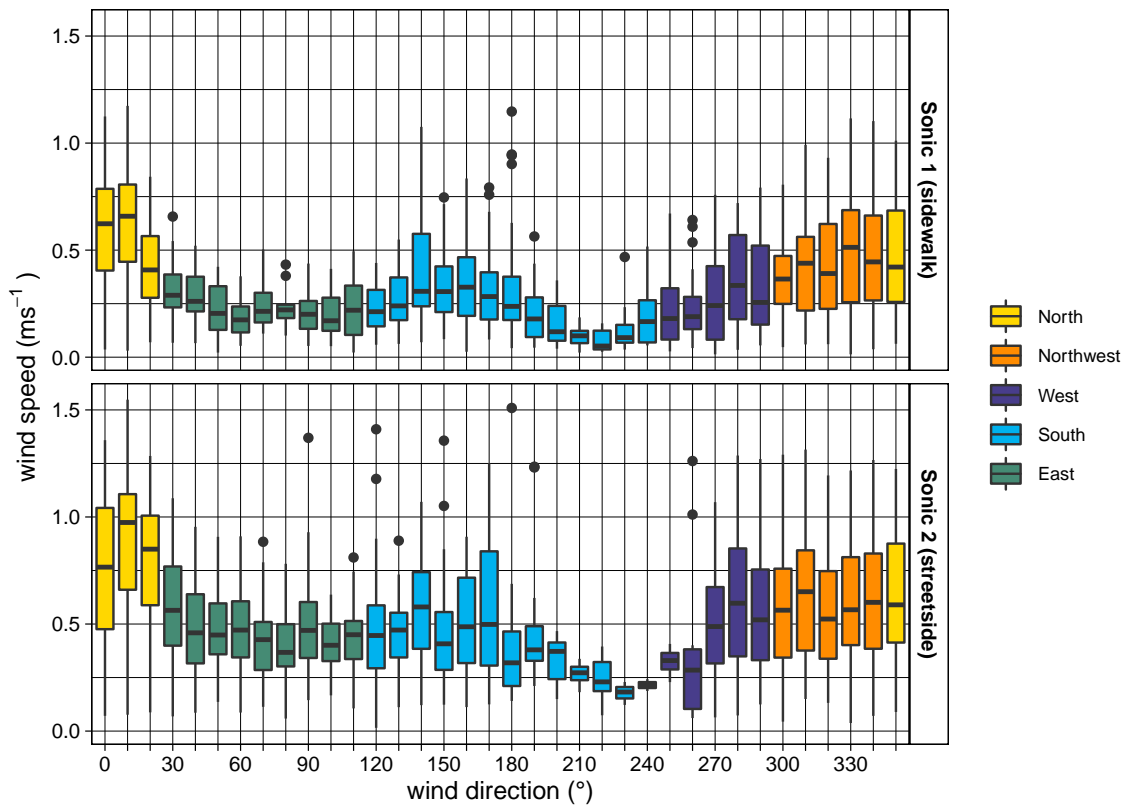


Figure 15.: Box plot of the wind speed for the sidewalk sonic (top panel) and the streetside sonic (bottom panel) divided by 10° wind direction sectors for the two-month observational period. The colors indicate the five predefined wind sectors "north", "northwest", "east", "south", "west". Boxplots are a standardized way of showing the distribution of quantitative data. The position and length of the box is determined by the upper and lower quartile. The line inside the box indicates the median. The whiskers extend 1.5 times the interquartile range (difference between the upper and the lower quartile) from the center of the box. All data points beyond the end of the whiskers are plotted individually as outliers.

The wind speed varied with wind direction (Figure 15). The wind speed was the highest for the flow channeled by the orientation of the street canyon: north and northwesterly flow. For these flow directions, the average wind speed was between 0.50 ms^{-1} and 1.0 ms^{-1} for the streetside sonic and between 0.40 ms^{-1} and 0.80 ms^{-1} for the sidewalk sonic. Lower wind speeds, with a median of around 0.5 ms^{-1} for the streetside sonic and a median of around 0.25 ms^{-1} for the sidewalk sonic, were observed for easterly and southerly flow. The weakest winds with median values of around 0.20 ms^{-1} for the streetside sonic and 0.10 ms^{-1} for the sidewalk sonic came from southeast.

3.1.2 Comparison with synoptic winds over Munich

In contrast to the Landshuter Allee, the wind in the Helene Weber-Allee came predominantly from west-southwest and east during the two-month observational period (Figure 16). In addition, the overall mean wind speed of 2.18 ms^{-1} was significantly higher compared to the Landshuter Allee. This is in line with the results of a report on the urban climate of Munich (Funk, 2014). This analysis showed that the longtime average wind conditions in Munich are dominated by west-southwesterly and easterly flow.

The direct comparison of the observed wind directions during the two-month measure-

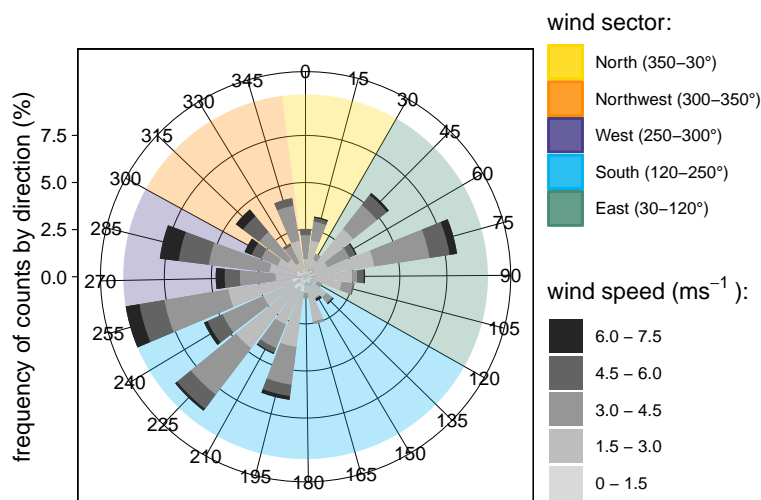


Figure 16: Wind rose plot illustrating the mean wind speed distribution per 15° wind sector at the DWD-operated meteorological station in the Helene-Weber Allee for the hourly observations during the two-month measurement period.

ment period illustrates that the wind conditions in the Landshuter Allee did not reflect the synoptic flow over Munich (Figure 17). Instead, the synoptic wind was mostly channelled to northerly winds aligned with the street orientation, independent of the synoptic flow direction. West wind in the Landshuter Allee only resulted from synoptic easterly flow and

3. Results and discussion

east wind in the street canyon mainly came from synoptic westerly flow. This leads to the conclusion that the synoptic wind from east and west is partially deflected by the building fronts and reversed in the street canyon (Figure 18) which confirms the findings of the previously conducted bachelor thesis that analyzed the flow regimes in the Landshuter Allee street canyon (Ramer, 2021).

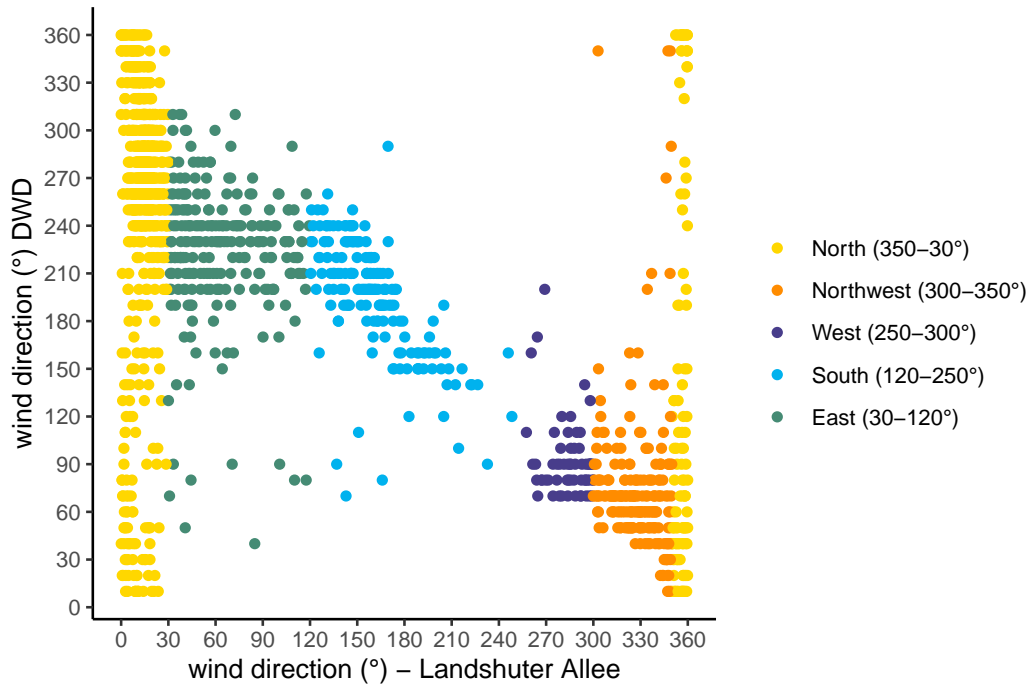


Figure 17.: Comparison of the measured wind direction during the two-month observational period for the LÜB-station in the Landshuter Allee and DWD-operated meteorological station in the Heinrich-Weber Allee. Each data point represents an hourly interval. The colors indicate the five predefined wind sectors "north", "northwest", "east", "south", "west".

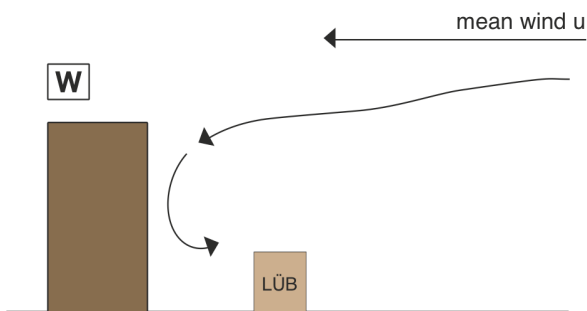


Figure 18: Presumed flow pattern in the Landshuter Allee street canyon when the synoptic easterly winds are reflected by the building fronts and reversed to westerly winds.

3.1.3 Atmospheric stratification

The atmospheric stratification in the Landshuter Allee was mostly unstable during the two-month observational period. The stability parameter ζ was smaller than -0.0625 for 86 % of all half-hourly data points (Table 7). Stable stratification occurred only sporadically, for 2 % of all half-hourly data points, and mainly at night when for 68 % of the half-hourly data points ζ was above 0.0625. Neutral stratification also did not occur often (12 %) and more frequently during the night (53 %). Overall, stable and neutral stratification were observed slightly more frequent for the sonic anemometer over the sidewalk (15 %) than for the sonic anemometer on the street-side (13 %) (Figure 19, top panel). The more detailed subdivision of the stability classes, depending on the magnitude of the stability parameter ζ illustrates the difference between both sonic anemometers (Figure 19, bottom panel). The proportion of half-hourly intervals with values for $\zeta < -1$ was comparatively higher for the sonic anemometer over the sidewalk. This indicates that the air surrounding the system was more often influenced by free convection with buoyancy as the main turbulence-generating process. In contrast, the sonic anemometer on the street side had a higher proportion of ζ values between -1 and -0.0625. The value range closer to neutral and unstable stratification suggests that the turbulence generation was more dependent on shear.

Table 7.: Overview of the total number of half-hourly intervals and the corresponding percentage of the respective stability regime depending on the sonic anemometer and the time of the day.

Stratification		Sonic 1 (sidewalk)	Sonic 2 (street-side)	Daytime	Nighttime
unstable	4950 (86%)	2377 (87%)	2573 (87%)	2932 (90%)	2018 (83%)
neutral	661 (12%)	322 (12%)	339 (12%)	310 (9%)	351 (14%)
stable	113 (2%)	83 (3%)	30 (2%)	36 (1%)	77 (3%)
	5724	2782	2942	3278	2446

Typically, the wind gradient near the surface increases after nightfall and radiative cooling constrains vertical turbulent motion. As a consequence, the atmosphere becomes increasingly stable and turbulent mixing is suppressed. In a street canyon, stable stratification can lead to an accumulation of air pollutants close to the source on the ground because the dispersive fluxes are capped. However, due to the UHI, unstable stratifica-

tion at night is a well-known phenomenon for the urban atmosphere (Pelliccioni et al., 2012) and could also be observed for the Landshuter Allee street canyon during the two-month measurement period. Due to the strong heating of urban surfaces, thermal convection is also present during the night. The atmospheric stratification rarely became stable for the two summer months and presumably did not impair the dispersion of air pollutants.

In general, there is a strong dependence of the stability on the seasonality because less solar radiation is received at the surface during the winter and the temperature profiles change. This leads to a more stable stratification, also in urban areas (Pelliccioni et al., 2012). The two-month observational period does not cover the full seasonality. It still showed the onset of the transition from summer to fall and the trend towards a more neutrally stratified atmosphere in the Landshuter Allee. For the first half of the measurement-period, 91 % of all half-hourly data points indicated unstable stratification, compared to 83 % in the second half. The percentage of neutral and stable stratification increased from 8 % to 14 % and from 1 % to 3 %, respectively. This shift towards a slightly more stable stratification suggests that the atmospheric stratification in the Landshuter Allee does show seasonality. With an increasingly stable stratification during the night in the winter months, the vertical turbulent motions potentially become more suppressed. However, this presumably also leads to increased nighttime wind speeds. These higher wind speeds have the potential to produce more turbulence compared to a weak-wind regime. The bachelor thesis of Ramer (2021) showed that the NO_2 concentration was higher in the summer compared to the winter. This supports the presumption that seasonal changes of the wind speed are the dominating process. Yet, a thorough analysis of one annual cycle of EC-measurements is required to gain better insight into the seasonality effects on the atmospheric stratification and the connection to the turbulence properties in the Landshuter Allee.

3.1. Characteristics of the flow and turbulence regime in the Landshuter Allee street canyon

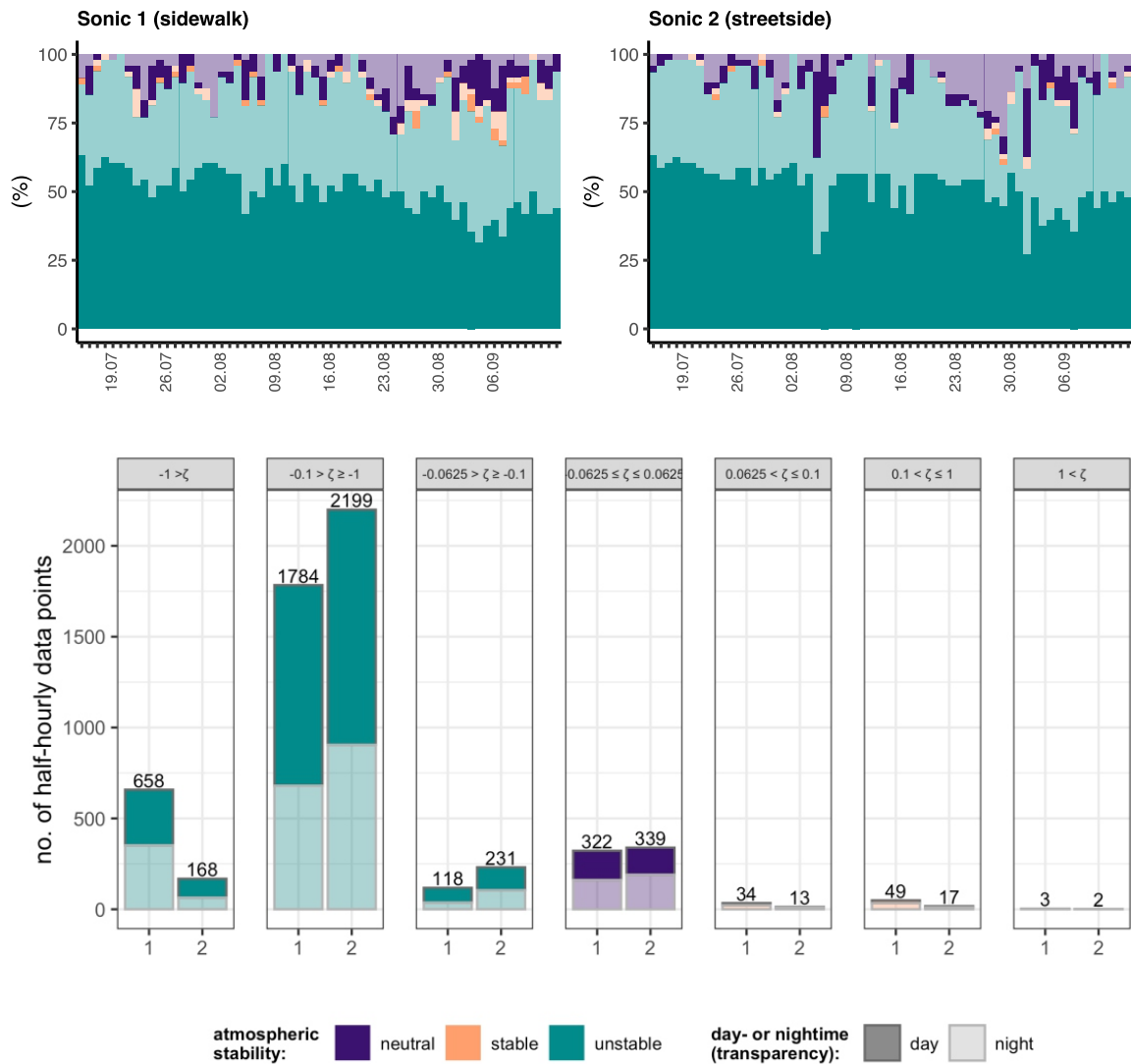


Figure 19.: Visualization of the atmospheric stratification in the Landshuter Allee during the two-month observational period.

Top: Daily percentage of half-hourly intervals of neutral (orange), stable (purple) and unstable (cyan) atmospheric stratification for the sidewalk sonic anemometer (left) and the streetside sonic anemometer (right).

Bottom: Number of data points per stability class for both sonic anemometers. Each data point represents one half-hourly interval. The stability classes of stable and unstable atmospheric stratification are further subdivided according to the size of the value of ζ (Table 4). The total number of intervals per sonic anemometer and stability range is written above the respective bar. The time of the day is represented by the transparency in both plots. High transparency illustrates nighttime and low transparency depicts daytime.

The average distribution of the Monin-Obukhov stability parameter ζ differed across the wind direction sectors (Figure 20). For both sonic anemometers, the median of ζ was closest to the range of -0.0625 to 0.0625. For the sidewalk sonic, the median of ζ was distinctly below -0.0625 for the other wind sectors. For the streetside sonic, the median

of ζ was also below -0.0625 but closer to the neutral range, especially for easterly flow. Overall, these findings need to be interpreted with caution. Since in the post-processing of the EC-data the vertical wind speed was not forced to zero, there might be a significant mean vertical wind speed that potentially reflects the buoyancy effects and falsifies the computation of the Monin-Obukhov stability parameter ζ .

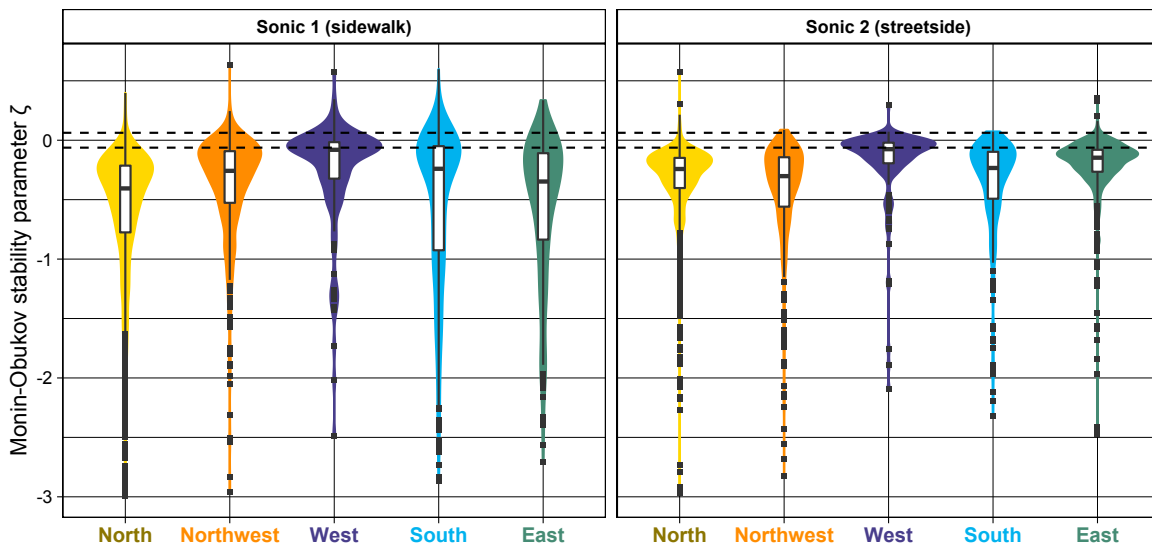


Figure 20.: Violin plot to illustrate the distribution of the Monin-Obukhov stability parameter ζ per flow regime and per sonic anemometer. The dotted lines correspond to $\zeta = -0.0625$ and $\zeta = 0.0625$ and mark the transition from unstable ($\zeta < -0.0625$) to neutral ($-0.0625 < \zeta < 0.0625$) to stable conditions ($\zeta > 0.0625$). The colors indicate the five wind direction sectors: "north" ($350^\circ - 30^\circ$), "northwest" ($300^\circ - 350^\circ$), "east" ($30^\circ - 120^\circ$), "south" ($120^\circ - 250^\circ$), "west" ($250^\circ - 300^\circ$). Compared to a box plot, the violin plot shows the full distribution of the data. The probability density is visualized on both sides of the boxplot.

3.1.4 Turbulent kinetic energy

The TKE is a measure to describe the energy associated with the eddy structures in turbulent flow and defines the flow behavior. During the two-month observational period, the TKE was in range of 0.012 to $1.9 \text{ m}^2\text{s}^{-2}$ in the Landshuter Allee street canyon. On average, the TKE was lower over the sidewalk ($0.21 \text{ m}^2\text{s}^{-2}$) compared to the streetside of the LÜB-Station ($0.29 \text{ m}^2\text{s}^{-2}$). As for the wind speed, the TKE varied with the time of the day and it was continuously higher on the streetside. The average ensemble diel of the half-hourly intervals showed a distinct course for both sonic anemometers (Figure 24). During the night, the TKE was only slightly above $0.0 \text{ m}^2\text{s}^{-2}$. It started

to increase at dawn and reached a plateau in the late morning hours with magnitudes around $0.30 \text{ m}^2 \text{ s}^{-2}$ for the sidewalk sonic and slightly below $0.50 \text{ m}^2 \text{ s}^{-2}$ for the streetside sonic. In the late afternoon, the TKE decreased again towards nightfall. The higher TKE values for the streetside sonic correspond to the higher wind speeds on the streetside and can potentially also be correlated with the closer proximity to the driving vehicles.

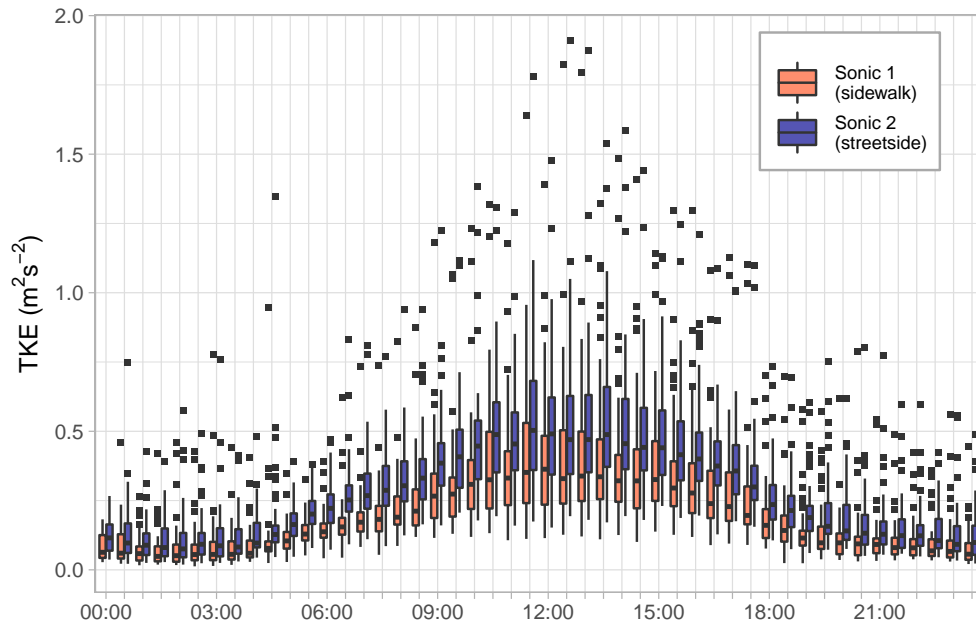


Figure 21.: Box plot illustrating the average ensemble diel for the half-hourly intervals of the the two-month measurement period of the TKE for the streetside sonic anemometer (blue) and the sidewalk sonic anemometer (red).

The TKE fluctuated considerably over the two-month observational period (Figure 22). The overall daily average for the streetside sonic was $0.26 \text{ m}^2 \text{ s}^{-2}$ compared to $0.17 \text{ m}^2 \text{ s}^{-2}$ for the sidewalk sonic. On most days, the daily median value was in the range of the overall daily average. Two days with higher median values stand out. On the 15.8. and the 2.9., the daily average of the TKE was above $0.40 \text{ m}^2 \text{ s}^{-2}$. The days following the 2.9. the median was again comparatively low, but the variability was high. In addition, there were several periods with a few days of comparatively low TKE median values and low variability (i.e. 26.8. to 31.8.). These trends were observed for both sonic anemometers during the measurement period and can presumably be correlated with the dominating wind direction on the respective day.

In general, the magnitude of the TKE was dependent on the wind direction. On average, the TKE was the highest for the northwest and west wind sector, similar for the north and

3. Results and discussion

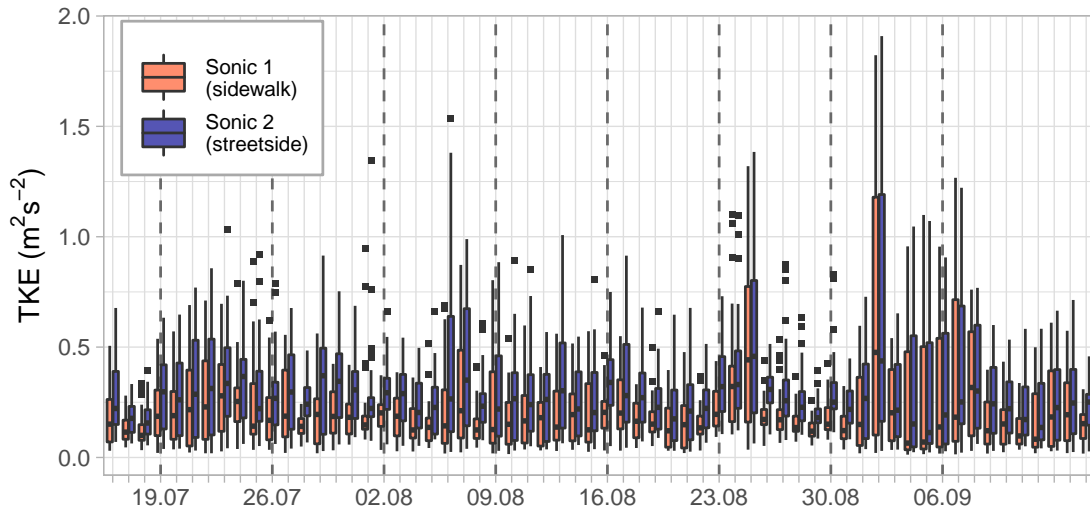


Figure 22.: Box plot of the TKE to illustrate the daily average for the street-side sonic (blue) and the sidewalk sonic (red) for the two-month observational period.

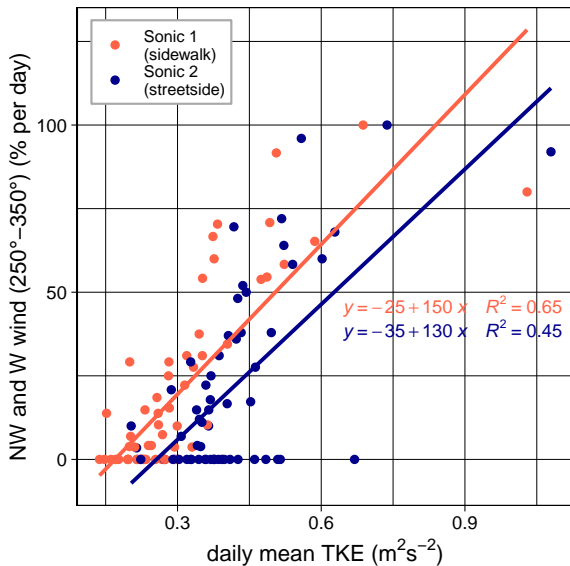


Figure 23: Daily percentage of westerly and northwesterly wind as a function of the daily mean TKE differentiated by sonic anemometer. Each data point represents one half-hourly interval of the two-month observational period. The solid lines correspond to the respective regression line with R^2 as coefficient of determination.

east wind sectors and the lowest for wind from the south (Figure 24). With an increasing percentage of northwesterly and westerly winds per day, the daily mean TKE increased (Figure 23). Therefore, the redirection of the synoptic easterly winds by the building fronts to westerly winds did not only lead to high wind speeds but also to the highest TKE during the observational period. The large deviation between the sidewalk and the streetside sonic for westerly winds is presumably caused by the flow-disturbing LÜB-station. For westerly winds, the streetside sonic measures the air that directly overflows the station which causes high values of TKE.

The presumption of a strong dependency of the TKE on the flow regime is additionally supported by the correlation of TKE and the mean wind speed \bar{u} (Figure 25). In general,

the TKE increased with increasing \bar{u} . This increase was most pronounced for westerly and northwesterly flow, resulting in higher TKE values compared southerly and northerly flow for the same mean wind speed. The stronger relative increase for easterly flow can likely be attributed to the traffic.

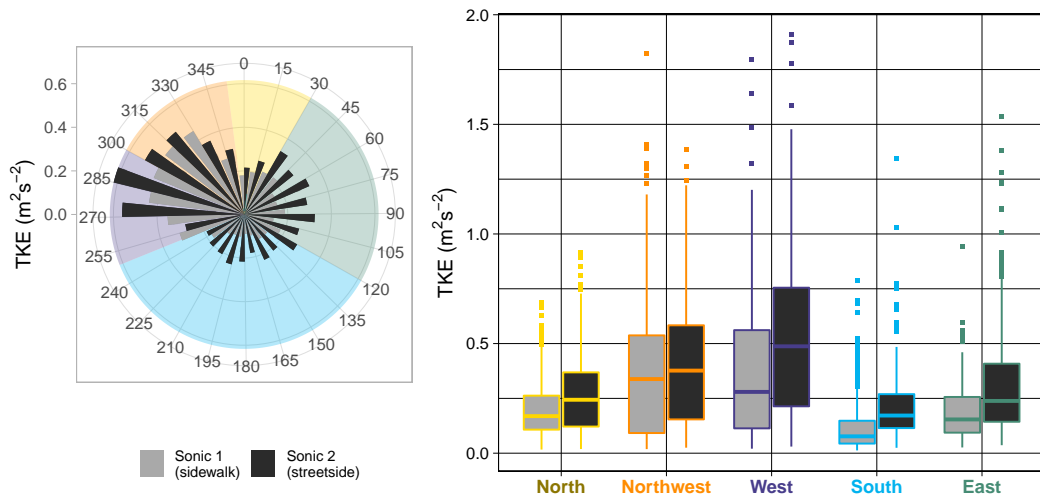


Figure 24.: Dependency of TKE on the wind direction. Left panel: Wind rose plot illustrating the mean TKE per 15° wind sector differentiated by sonic anemometer. Right panel: Box plot showing the average TKE per predefined wind sector. The wind sectors "north" (350°–30°), "northwest" (300°–350°), "east" (30°–120°), "south" (120°–250°) and "west" (250°–300°) are differentiated by color.

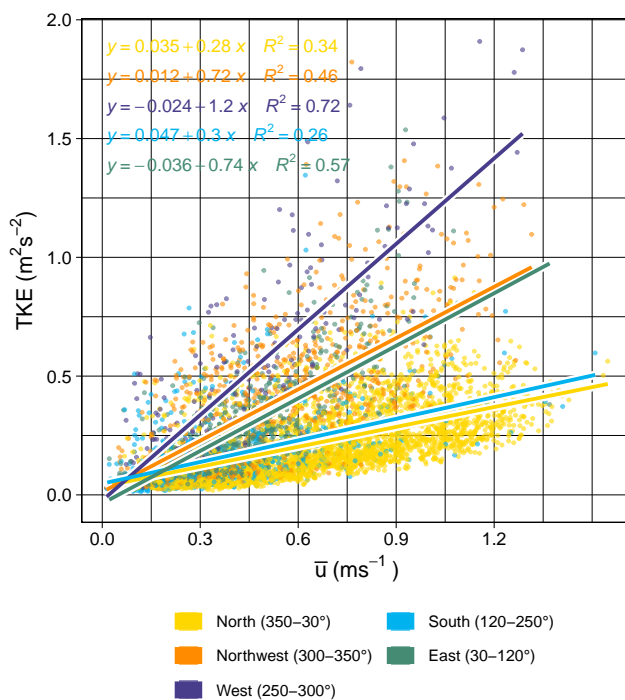


Figure 25: TKE as a function of the mean wind speed \bar{u} . Each data point represents one half-hourly interval of the two-month observational period. The flow regimes are differentiated by color and the solid lines correspond to the respective regression line with R^2 as coefficient of determination.

3.1.5 Contributions to the TKE tendency

The TKE budget equation (Eq. 2.3.14) is commonly investigated to analyze which atmospheric processes contribute to the consumption or production of TKE. Two terms of the TKE budget equation are examined and compared in this study: the shear generation term and the buoyancy production term. Both terms were generally larger for the streetside sonic during the two-month observational period (Figure 26). Overall, the shear generation was the dominant source of TKE throughout most of the day for the streetside sonic while for the sidewalk sonic the buoyancy term did not differ significantly from the shear term. The mean buoyancy production over the entire measurement period was $1.8 \cdot 10^{-3} \text{ m}^2\text{s}^{-3}$ for the street-side sonic and $1.4 \cdot 10^{-3} \text{ m}^2\text{s}^{-3}$ for the sidewalk sonic, the corresponding values for the mean shear generation were $3.7 \cdot 10^{-3} \text{ m}^2\text{s}^{-3}$ and $2.5 \cdot 10^{-3} \text{ m}^2\text{s}^{-3}$, respectively. The ensemble averaged diel of the buoyancy produc-

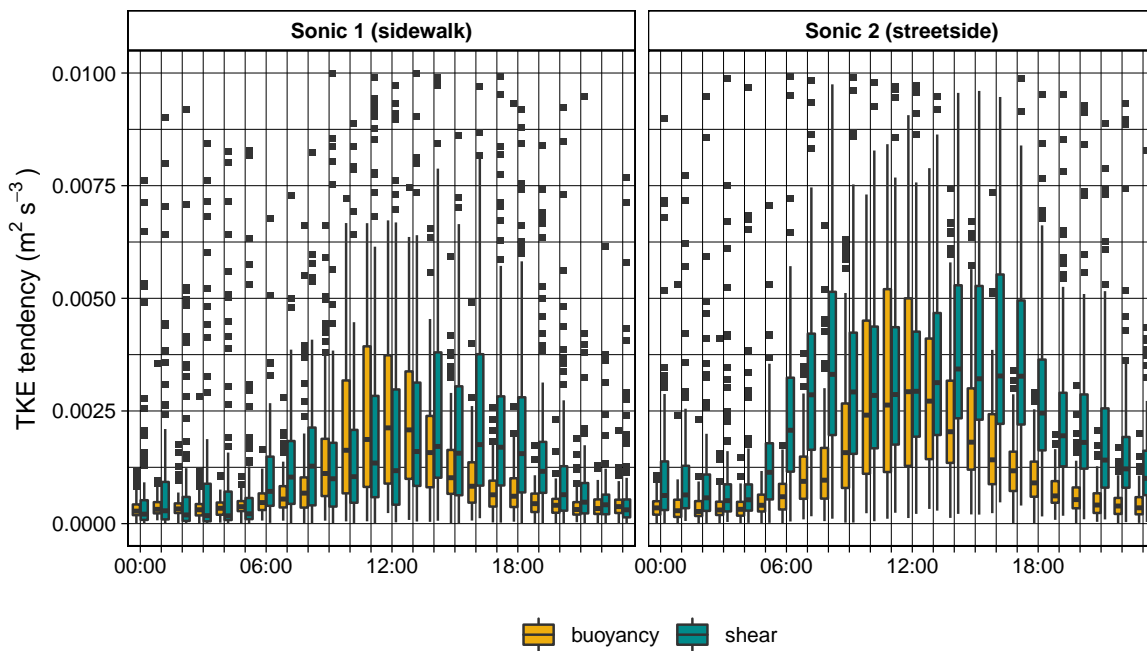


Figure 26.: Boxplot illustrating the ensemble averaged diel for the half-hourly intervals of the buoyancy production (yellow) and shear generation term (cyan) in the TKE budget equation for the sidewalk sonic anemometer (left panel) and the streetside sonic anemometer (right panel).

tion and shear generation term in the TKE budget equation showed a distinct diurnal course during the measurement period (Figure 26). During the night, buoyancy and shear had the smallest magnitude with values only slightly above zero. The diurnal course of the buoyancy term was similar for both sonic anemometers. The buoyancy

3.1. Characteristics of the flow and turbulence regime in the Landshuter Allee street canyon

term began to increase in the early morning hours, reached the peak shortly before noon and decreased again towards nightfall. The peak of the buoyancy term was approximately $0.7 \cdot 10^{-3} \text{ m}^2\text{s}^{-3}$ higher on the streetside compared to the sidewalk. The diurnal course of the shear contribution differed between the two sonic anemometers. On the streetside, the shear term strongly increased after dawn and reached a steady level from the early morning until the late afternoon, when it began to decrease slowly towards midnight. Over the sidewalk, the shear contribution also started to gain influence after dawn but increased slower compared to the streetside. The shear term reached its maximum in the late afternoon and was approximately $2.2 \cdot 10^{-3} \text{ m}^2\text{s}^{-3}$ lower than on the streetside. While the magnitude of the buoyancy and shear term was similar for both sonic anemometers during the night, during the day, the buoyancy production was on average 42 % and the shear production on average 51 % larger on the streetside. The difference between the two sonic anemometers goes in line with the difference in total TKE and can presumably be attributed to the higher wind speeds on the streetside.

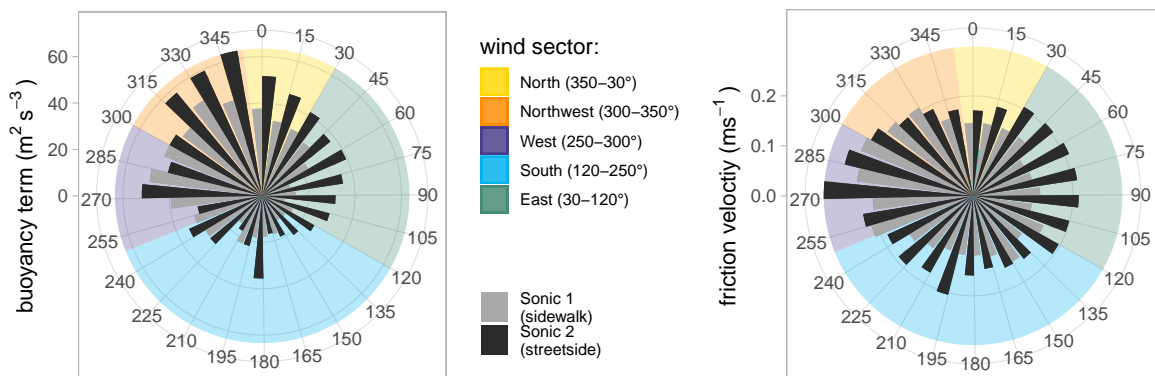


Figure 27.: Wind rose plots for the two-month observational period illustrating the mean buoyancy flux H (left panel) and the mean friction velocity u_* (right panel) per 15° wind sector differentiated by sonic anemometers. The five wind sectors "north", "northwest", "east", "south" and "west" are highlighted by color.

The computation of the buoyancy term was based on the measured buoyancy flux H and the shear term was determined using the friction velocity u_* . The magnitudes of u_* and H fluctuated with wind direction during the the two-month observational period (Figure 27). On average, H and u_* were higher on the streetside. For both measuring systems, H was the highest for northwesterly winds, with a mean of 59 Wm^{-2} for the streetside sonic and 44 Wm^{-2} for the sidewalk sonic, while u_* was the highest for westerly winds

3. Results and discussion

with the corresponding mean values of 0.26 ms^{-1} and 0.23 ms^{-1} . Over the sidewalk, u_* was second highest for northwesterly winds (0.19 ms^{-1}) and similar for the other wind sectors ($\approx 0.14 \text{ ms}^{-1}$). In contrast, on the street-side, u_* was comparatively higher for easterly winds (0.21 ms^{-1}) in relation to winds from northwest, north and south. For both sonic anemometers, H was higher for northerly, northwesterly and westerly winds, compared to winds from south and east.

The overall high mean u_* for westerly flows goes in line with the findings, that turbulence was stronger for wind that was deflected by the building fronts. The comparatively high mean u_* on the streetside for easterly flow can likely be explained by the influence of the traffic. Because u_* was not enhanced for easterly flow for the sidewalk sonic, the influence of traffic seemed to more significant on the streetside. H was the largest for winds that come from near the buildings. This supports the assumption that buildings and the LÜB-Station, as additional source for heat input, enhance the effect on the buoyancy.

3.2 Comparison of street-typical north wind period and west wind dominated period

The flow regime in the Landshuter Allee street canyon was dominated by northerly winds that align with the street orientation. However, if west wind occurred in the street canyon, the wind speeds and the TKE was the largest. These differences have a significant impact on the street ventilation and pollution dispersion. To investigate this in more detail, two 48 h periods are compared: one representing the site-typical north wind flow regime and one with west wind dominated conditions (Figure 28). During the measurement period there were several days with a high daily contribution of westerly and northwesterly wind. On Tuesday, the 7.9.21 and Wednesday, the 8.9.21, the percentage of west wind was high for two consecutive days. On these two days, 51 % and 92 % of the wind came from north and northwest while only 40 % and 6.0 % of the wind came from north. In contrast, on Tuesday, the 20.7.21 and Wednesday, the 21.7.21 the percentage of north wind was 87 % and 82 %.

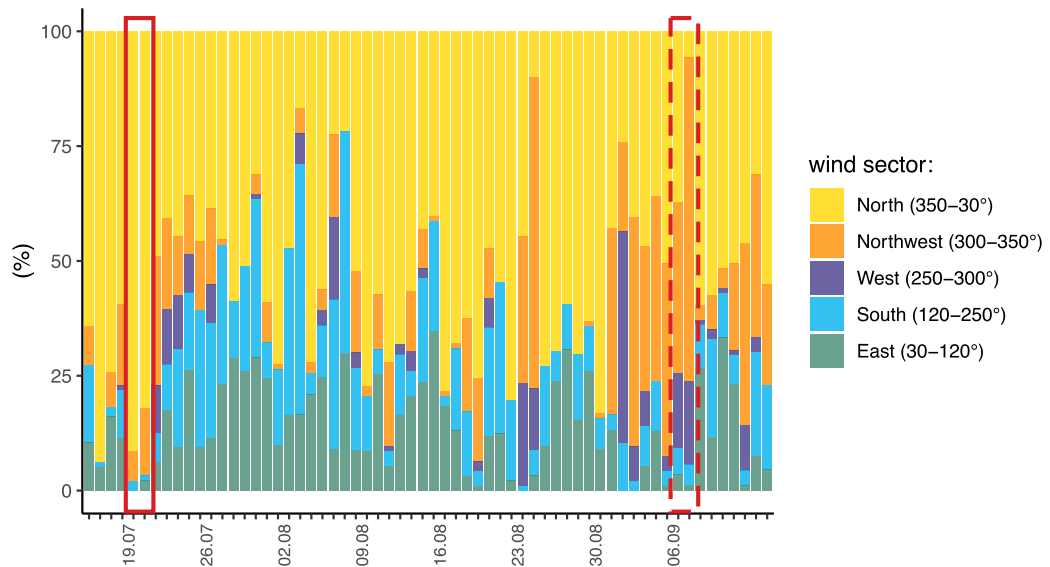


Figure 28.: Percentage per wind sector as daily mean for both sonic anemometers. The five predefined wind sectors "north", "northwest", "east", "south" and "west" are differentiated by color. The two 48h time periods that represent the site-typical north wind (20. and 21.7.) and west wind dominated conditions (7. and 8.9.) are framed by red boxes.

During the 48 h west wind period in September, north wind mainly occurred during the night and in the early morning hours and during daytime the flow regime was dominated by winds mainly from northwest (Figure 29). During the north wind period in July, the proportion of northwesterly wind increased from the first to the second measurement

3. Results and discussion

day. The northwesterly wind occurred mostly in the afternoon. The wind speed was in the range of 0.15 ms^{-1} to 1.0 ms^{-1} for both 48 h periods and showed a similar diurnal course. While the maximum value was slightly below 1.0 ms^{-1} for both measurement days, the daily mean wind speed was lower for the second measurement day compared to the first day. Overall, the wind speed was slightly higher during the north wind period in July with a mean wind speed of 0.53 ms^{-1} compared to the mean wind speed of 0.45 ms^{-1} for the west wind period.

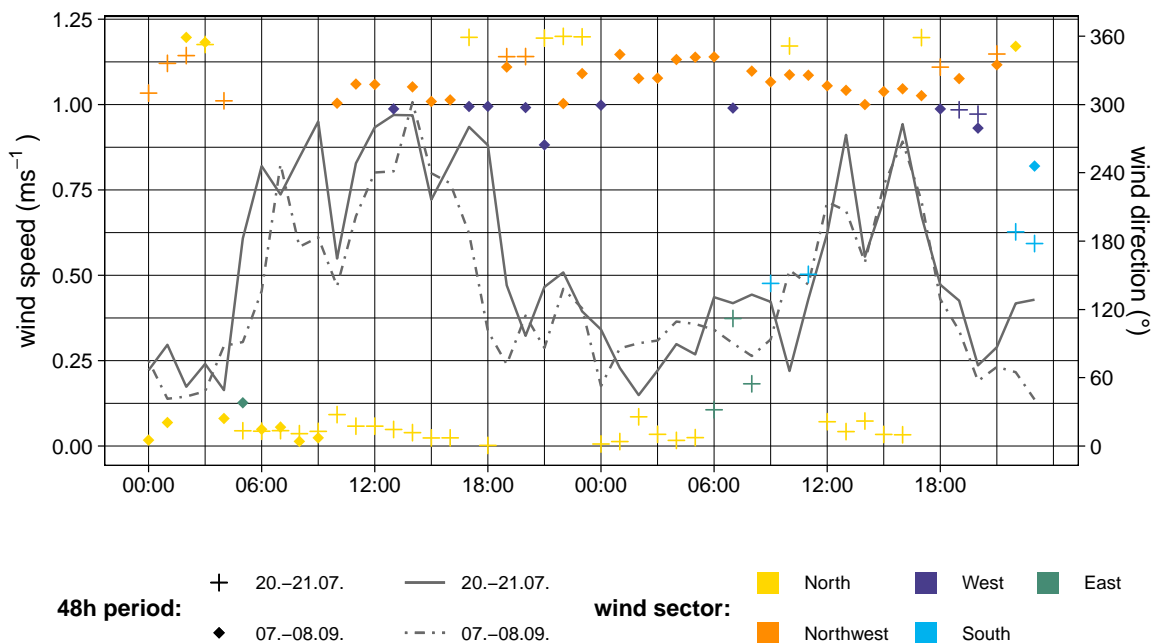


Figure 29.: Time series plot of the hourly mean wind speed and wind direction for the two 48 h time periods that represent site-typical north wind (20. and 21.7.) and west wind dominated conditions (7. and 8.9.). The wind speed is displayed as solid (20. and 21.7.) and dashed line (7. and 8.9.). The wind direction is represented by single points - crosses (20. and 21.7.) and diamonds (7. and 8.9.) - and further differentiated by color. The colors indicate the five predefined wind sectors "north" ($350^\circ - 30^\circ$), "northwest" ($300^\circ - 350^\circ$), "east" ($30^\circ - 120^\circ$), "south" ($120^\circ - 250^\circ$), "west" ($250^\circ - 300^\circ$).

Apart from wind speed and direction, solar radiation (*SR*) and the air temperature also play an important role for the turbulence regime. The amount of solar radiation, that reaches the surface is influenced by seasonality, the synoptic forcing and the morphology of the street canyon. The building geometry and the presence of urban trees can lead to shading effects dependent on the time of the day. The higher number of daylight hours during the north-wind period in July resulted in a longer diurnal time span of a *SR* and higher peak values (Figure 30). For both 48 h periods the *SR* dropped slightly

3.2. Comparison of street-typical north wind period and west wind dominated period

around noon due to a large tree crown directly south of the instruments. The buoyancy flux directly relates to the SR . H was on average slightly higher during the west wind period in September with a mean of 43.3 Wm^{-2} compared to 39.9 Wm^{-2} during the north wind period. During the north wind period in July, H peaked approximately two hours later in the day, reaching a maximum value of 145 Wm^{-2} at noon on the second day. In September the maximum value of 215 Wm^{-2} was also reached on the second day.

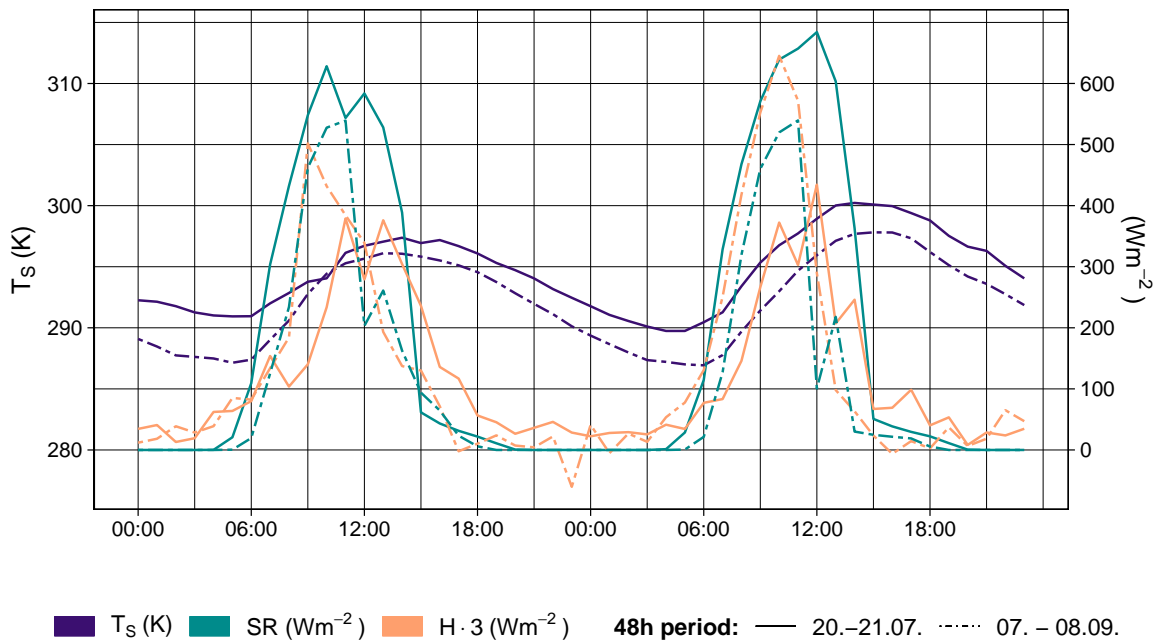


Figure 30.: Time series plot of the hourly mean solar radiation SR (green), the sonic temperature T_s (purple) and the buoyancy flux H (orange) for the two 48 h time periods that represent site-typical north wind (20. and 21.7.) and west wind dominated conditions (7. and 8.9.). H is scaled by a factor of three. The north wind period is displayed as solid line and the west wind period as dashed line.

The temperature measured by the sonic anemometers is not equal to the absolute air temperature. The sonic temperature closely approximates the virtual temperature T_v . T_v describes the temperature of a dry air parcel if it had the same density as a moist air parcel. As a consequence, T_v can be greater than the absolute air temperature in unsaturated moist air. However, for an urban street canyon with low humidity, the difference is expected to be insignificant. The sonic temperature T_s was in the range of 290 K to 300 K during the north wind period in July and slightly lower, between 287 K and 298 K, during the west wind period in September. The diurnal course was similar for

3. Results and discussion

both 48 h periods with a systematic difference of approximately 3 K. Only on the first day at around 10:00, the T_S of the northwind period dropped below the T_S of the west wind period.

The diurnal course of the total TKE as well as the buoyancy and the shear contribution to the TKE budget equation varied during the north wind period in July and the west wind period in September 31. During the west wind period, the TKE was significantly higher on the first measurement day compared to the second day. This was opposite during the north wind period, where the TKE was slightly higher on the second measurement day. Overall, the TKE was mostly larger during the west wind period, but the difference was more pronounced on the first measurement day. The difference in the daily maximum TKE was $0.6 \text{ m}^2\text{s}^{-2}$ compared to $0.1 \text{ m}^2\text{s}^{-2}$.

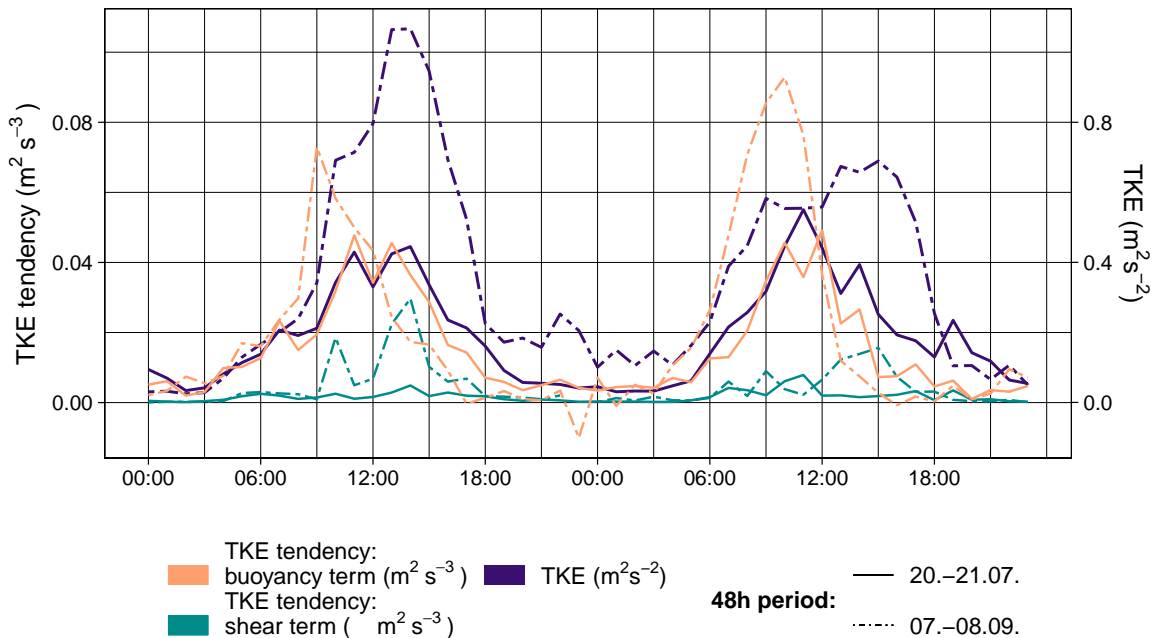


Figure 31.: Time series plot of hourly mean of the buoyancy (orange) and the shear (green) contribution to the TKE budget equation and the total TKE (purple) for the two 48h time periods that represent site-typical north wind (20. and 21.7.) and west wind dominated conditions (7. and 8.9.). The north wind period is displayed as solid line and the west wind period as dashed line.

The higher TKE on the first measurement day of the west wind period can potentially be explained with the higher mean wind speed on the first day compared to the second day. As shown in section 3.1.4, TKE and \bar{u} can be linearly correlated. With increasing \bar{u} , the TKE increases. This increase was most pronounced for the west wind sector (Figure 25). During the west wind period, \bar{u} decreased from the first to the second day

and and so did the TKE. In contrast, during the north wind period this correlation was not observed. While \bar{u} decreased, the TKE slightly increased from the first to the second measurement day. However, the percentage of northwesterly and westerly wind per day increased from 7 % to 15 % from the first to the second day (Figure 28). In general, the increase in TKE with increasing \bar{u} was least pronounced for the north wind sector (Figure 23) while the TKE increased strongly with increasing percentage of westerly and northwesterly wind per day. Therefore, the increase in northwesterly wind seemed to be the dominating factor for the diurnal course of the TKE during the north wind period.

In contrast to the ensemble average diel of the TKE tendency over the entire measurement period (Figure 26), the buoyancy term was continuously higher than the shear term for both 48 h time periods. Both buoyancy and shear term were higher during the west wind period throughout most of the day. The shear term remained close to zero for the north wind period both at daytime and nighttime and peaked twice with varying magnitude at around 10:00 and 14:00 on both days during the north-wind period.

The overall higher values for buoyancy compared to shear are partially linked to the low wind speeds for both 48 h periods. The overall mean wind speed of 0.57 ms^{-1} for the two-month measurement period was higher than the wind speed during both north and west wind period with corresponding mean values of 0.53 ms^{-1} and 0.45 ms^{-1} . The lower the wind speed, the lower is the potential for wind-shear induced turbulence. In contrast, the *SR* during both 48 h periods indicated clear-sky conditions which likely intensified thermal convective processes and enhanced the buoyancy flux. The combination of a small shear term and comparably large buoyancy term potentially explain why the buoyancy term was higher than the shear term for the two 48 h periods in contrast to the entire measurement period.

3.3 Influence of traffic on the turbulence regime

3.3.1 Traffic in the Landshuter Allee

The ensemble averaged diel of the half-hourly vehicle count showed typical commuter traffic for the weekdays (Figure 32). Starting at 5:00, the vehicle count increased strongly from only 20 to slightly under 600 vehicles each half-hour by 8:30. The morning rush hour ended at 9:00 and afterwards, the traffic intensity remained at a level of approximately 500 vehicles per half-hour until the afternoon. The afternoon rush hour started at around 14:00 and the vehicle count increased to over 600 vehicles per half-hour. After 19:00 the vehicle count fell steadily until the morning hours. On the weekends, there was no distinct rush hours. The vehicle count increased more slowly in the morning, reached a maximum of about 490 vehicles per half-hour at noon and decreased afterwards towards the evening.

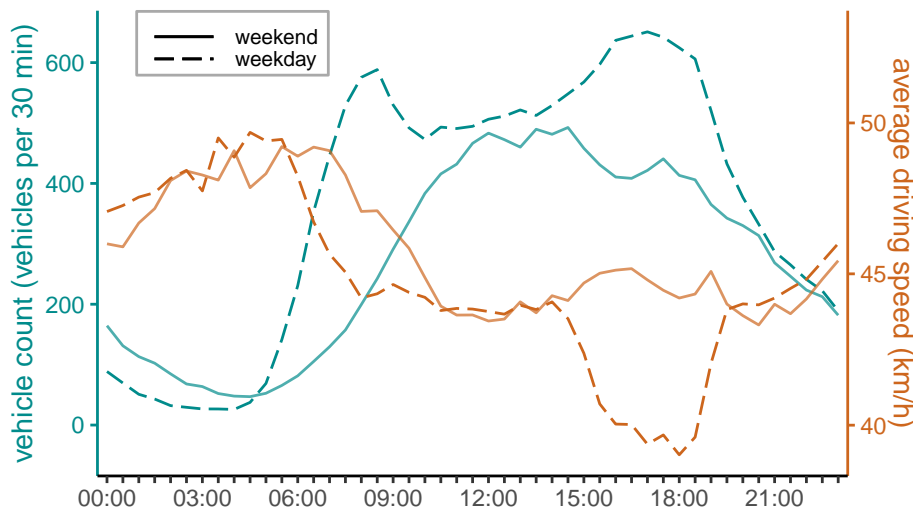


Figure 32.: Ensemble average diel of the traffic volume (orange) on the two driving lanes directly adjacent to the LÜB-station station and the associated mean driving speed (cyan) for the two-month time period from the 16.07.2021 to the 15.09.2021 divided by day of the week. The dotted line shows the ensemble average for the weekend (Saturday and Sunday) and the solid line the average for the weekdays (Monday through Friday).

The ensemble average of the mean driving speed also followed a distinct diurnal course for weekdays and the weekend. The driving speed was in the range of 38 to 50 km/h which falls within the permitted speed limit of 50 km/h. During the night, the driving speed was comparatively higher than during the day. With the onset of increasing traffic inten-

sity in the morning, the driving speed decreased. For the weekends, the driving speed remained constant but during the week there was a significant drop below 40 km/h during the afternoon rush hour.

The nine vehicle categories were summarized into two main categories: "truck-like" and "car-like" vehicles (Table 5). Overall, significantly more car-like vehicles were counted during the two-month measurement period (Figure 33, right panel). The average vehicle count per day was different across weekday and weekend. During the week the average count for the "car-like" category was 4,841 vehicles per day and 525 for the "truck-like" vehicles. Both car-like and truck-like vehicles decreased in number on the weekends with an average vehicle count per day of 3,463 for car-like and 293 for truck-like vehicles. With $\approx 45\%$ less vehicles per day on the weekends, the decrease in vehicle count was more pronounced for the truck-like vehicles. The average vehicle count for the car-likes vehicles decreased by 29%.

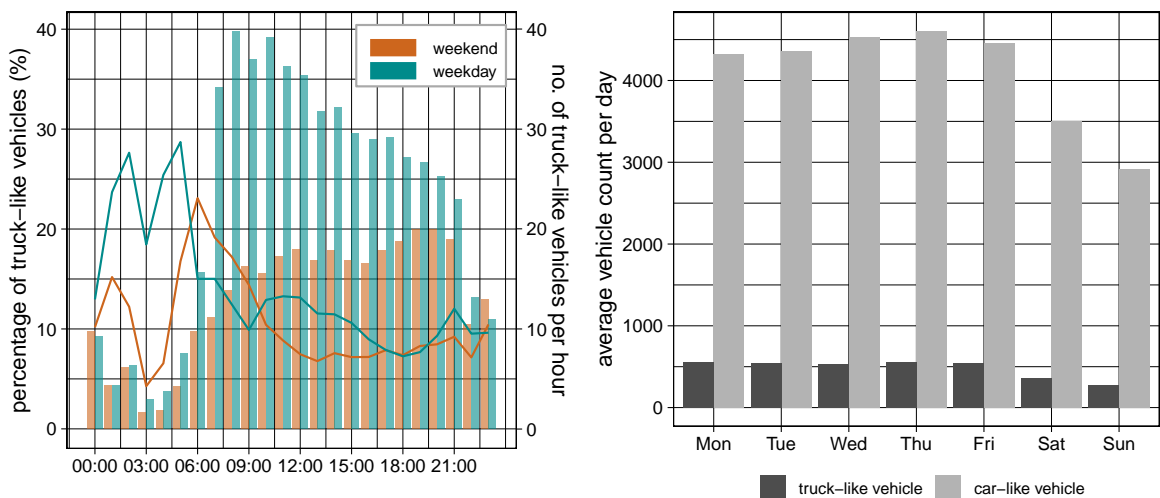


Figure 33.: Distribution of the vehicle types for the two south-orientated driving lanes closest to the LÜB-station station over the course of the two-month observational period. Left panel: Diurnal ensemble average of the percentage (lines) and the total number (bars) of truck-like vehicles per hourly interval differentiated by weekday (cyan) and weekend (orange). Right panel: Distribution of the vehicle count per day in the week in the two main categories "truck-like" (darkgrey) and "car-like" (lightgrey). Each day occurred equally often during the measurement period.

Over the course of the day, the percentage of truck-like vehicles varied (Figure 33, left panel). On average, the share of truck-like vehicles was larger during the night and in the early morning hours while the total number of truck-like-vehicles per hour was

consistently below 40. Both on the weekdays and on the weekend, the percentage of truck-like vehicles peaked around 1:00 in the morning. During the week, there was a second peak shortly before the morning rush hour and on the weekend, the percentage peaked again at around 6:00. During the day, the percentage of truck-like vehicles was steadily around 10 %.

3.3.2 Turbulence characteristics

The traffic data for the Landshuter Allee showed typical commuter traffic for the weekdays with high traffic intensities especially during the rush hours and a lower traffic intensity for the weekends. To investigate the influence of traffic on the turbulence regime, it is therefore reasonable to analyze the differences in the turbulence characteristics depending on the day of the week. Overall, 18 days of the measurement period fell on the weekend and 44 days on a weekday.

Table 8.: Overview of the mean TKE (m^2s^{-2}) over the entire two-month observational period, separated by the sonic anemometer, the day of the week and only the daytime.

sonic anemometer	overall	weekend	weekday	weekend (daytime)	weekday (daytime)
sidewalk sonic	0.22	0.19	0.23	0.26	0.32
streetside sonic	0.30	0.26	0.31	0.34	0.43
overall	0.26	0.22	0.27	0.30	0.38

Vehicle-induced turbulence (VIT) can be a major mechanism for turbulence generation in a traffic-influenced urban environment. The VIT can significantly contribute to the buoyancy production and shear generation of TKE. In contrast to idealized flow models, the sonic anemometers report the total TKE and cannot accurately partition the TKE into the different sinks and sources. However, the TKE measurements in the Landshuter Allee still showed the influence of VIT on the TKE's diurnal course (Figure 34). Overall, the TKE was higher for the street-side sonic, independent of the day of the week. The TKE was consistently low during the night, both on the weekends and during the week. In the morning, the increase in TKE started earlier on the weekdays in correspondence to the morning rush hour at 5:00. On the weekends, the increase in TKE lagged by

approximately 2 h compared to the weekdays. The mean daily maximum of the TKE was reached in the late morning at around 11:00 for both measuring systems. Although the TKE peaked on average at the same time across all days of the week, the magnitude of the difference between the weekdays and the weekends varied. On the weekends, the maximum values were approximately 22 % lower for the streetside sonic and about 9 % lower for the sidewalk sonic compared to the weekdays. On the weekdays, the decrease in TKE towards nightfall lagged by approximately 1h compared to the weekend. Overall, the TKE began to increase earlier in the day reached a larger peak and started to decrease later. This led to higher mean TKE values on weekdays which was more pronounced during daylight hours compared to nighttime (Table 8). These differences can be attributed to the higher traffic intensity on the weekdays and the proximity of the streetside sonic to the traffic.

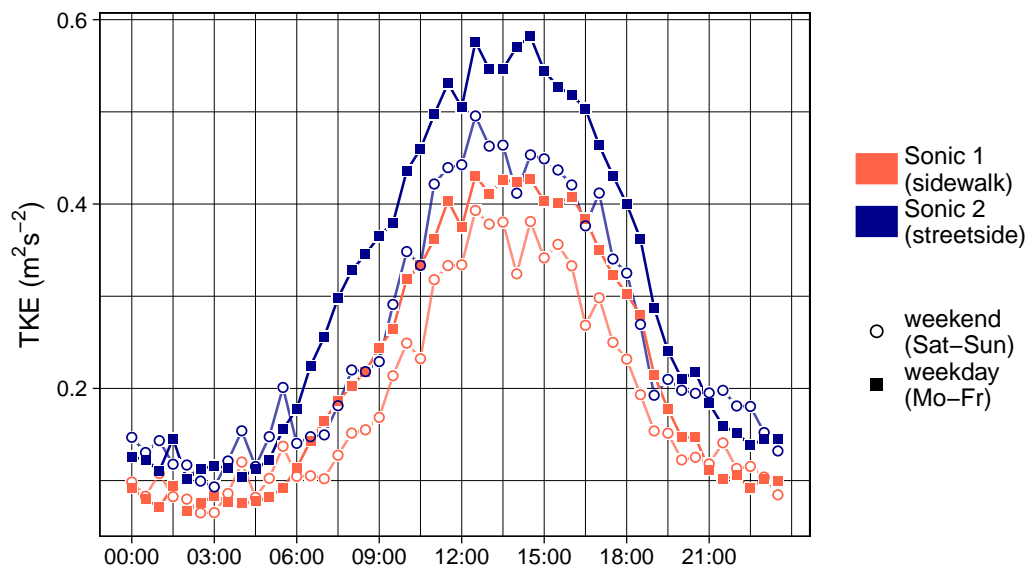


Figure 34.: Ensemble average diel of the TKE for the given half-hour intervals over the two-month observational period. Depicted is the average per measuring system (sidewalk and streetside sonic) with further subdivision by the day of the week (weekdays and weekend).

3.3.2.1 Influence of traffic on the TKE tendency

The VIT potentially influences both buoyancy and shear term in the TKE budget equation. Across the two-month measurement period, the median ratio of shear to buoyancy was significantly larger than unity for the streetside sonic while it equalled unity for the sidewalk sonic (Figure 35, left panel). The comparatively higher shear to buoyancy ratio

3. Results and discussion

on the streetside supports the findings, that the shear contribution to the TKE was higher on the streetside due to the higher wind speeds and the close proximity to the moving vehicles.

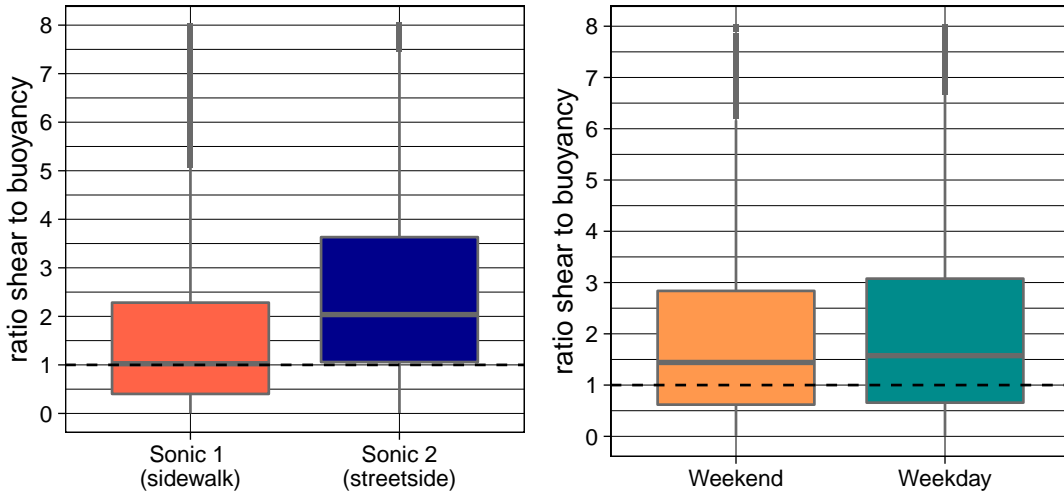


Figure 35.: Boxplot illustrating the overall ratio of the shear to the buoyancy term in the TKE budget equation depending on the measuring sonic anemometer (left) and depending on the day of the week (right).

The contribution of buoyancy and shear to the TKE budget equation fluctuated depending on the time of the day but showed a similar diurnal course for both weekend and weekdays (Figure 36). The median of the ratio of buoyancy to shear was around unity at nighttime and over midday. During the early morning hours and in the afternoons, the ratio clearly exceeded unity with maximum median values of 2.9 on the weekdays and 2.0 on the weekends.

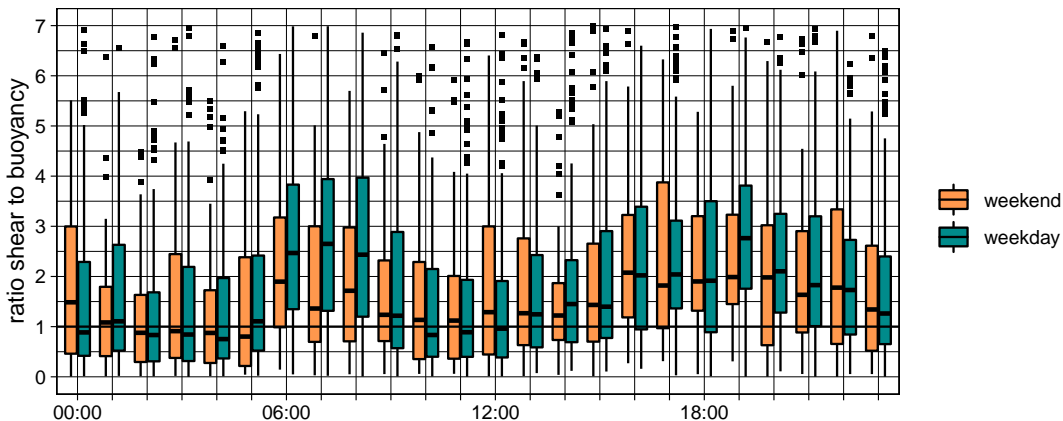


Figure 36.: Boxplot illustrating the ensemble average diel of the hourly shear to buoyancy ratio as an average for both sonic anemometers. The ratio of the terms in the TKE budget equation was further subdivided by weekday (cyan) and weekend (orange). Unity is indicated as solid line.

During the night, the buoyancy to shear ratio was around unity because the buoyancy and the shear term were similarly low but not zero. The increase in shear contribution occurred parallel to the increase in wind speeds in the morning resulting in shear to buoyancy ratios that clearly exceeded unity. Over noon, when the SR was the highest, the shear production was presumably counteracted by the increasing influence of buoyancy. In the afternoons, the shear to buoyancy ratio again exceeded unity, likely because the SR decreased while there were still significant wind speeds. Consequently, the wind induced shear was again the dominant turbulence generating mechanism. No significant differences in the shear to buoyancy ratio were observed depending on the day of the week both in the overall average (Figure 35, right panel) and the ensemble average diel (Figure 36) even though the traffic intensity was significantly higher on the weekdays. The unique influence of the VIT on the thermal-induced and wind-shear induced turbulence could therefore not be distinctly separated.

3.3.2.2 Influence of vehicle count, driving speed and vehicle type on TKE

There was a strong linkage between the TKE and the number of vehicles per 30 min interval (Figure 37, left panel). The vehicle count was in the range of 0 to 800 during the two-month observational period. Half-hourly intervals with 300 vehicles and less were associated with low TKE values. These vehicles counts mostly occurred during the night and in the early morning hours. Starting at 300 vehicles per 30 min interval, the TKE increased with increasing vehicle count. The majority of the data points fell within the range of 400 to 600 vehicles per 30 min interval. This range was typical for the average daytime traffic intensity. The TKE was the largest for a vehicle count of approximately 500. Above this threshold, the TKE decreased with increasing vehicle count. A traffic intensity of 600 vehicles per 30min and above was partially reached during the morning rush-hour and mostly during the afternoon rush-hour. These findings agree with a previous study (Vachon et al., 2002). They showed that the TKE increases with increasing traffic up until a certain threshold. Above this threshold, the vehicles are closer together and the driving speed decreases. This leads to traffic congestions, resulting in a blocking effect and consequently in a decrease in TKE. For the Landshuter Allee, this was the case during the afternoon rush-hour.

3. Results and discussion

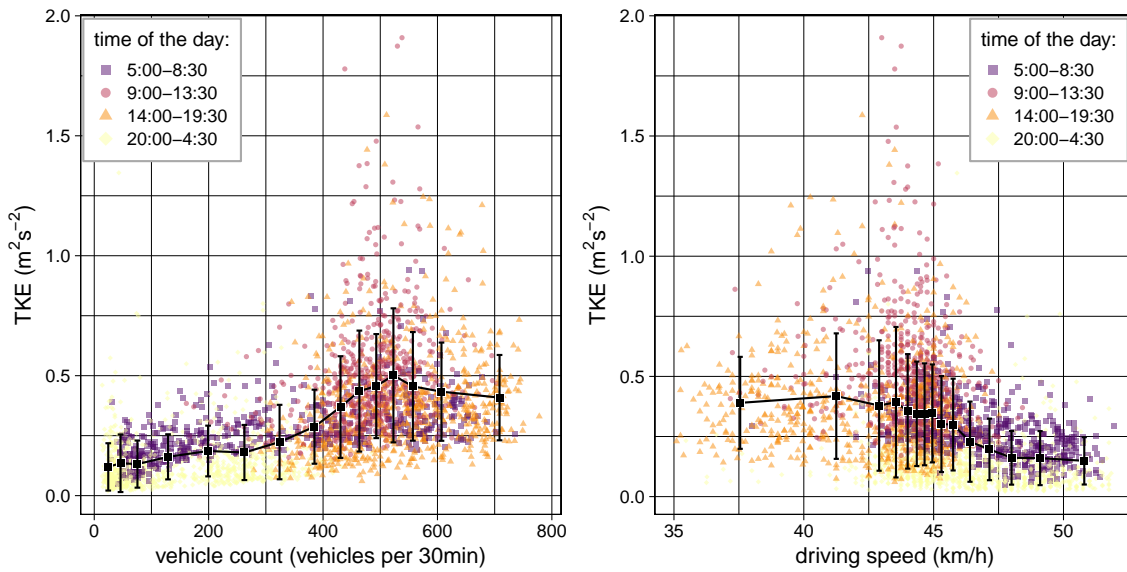


Figure 37.: TKE as a function of the number of vehicles per 30 min interval (left) and as a function of the mean driving speed per 30 min interval (right). The data intervals for the two-month measurement period are categorized by the time of the day: 5:00-8:30 (purple squares), 9:00-13:30 (red circles), 14:00-19:30 (orange triangles) and 20:00-4:30 (yellow diamonds). Dynamic bin averages are illustrated in black and the error bars denote \pm one standard deviation.

The mean driving speed ranged from 38 to 50 km/h over the course of the two-month measurement period (Figure 37, right panel). High driving speeds occurred mostly during the night and in the early morning and were observed along with low TKE values. The TKE was comparatively higher during the day with most data intervals with a mean driving speed in the range of 43 to 46 km/h. Intervals with lower driving speeds mainly occurred during the afternoon rush-hour but were not associated with significantly lower TKE values. The highest driving speeds in the Landshuter Allee occurred during the night and in the mornings, where the TKE is in general the lowest because of overall low wind speeds and the thermal forcing. Apart from the nighttime values, the TKE was similar for all driving speeds. The missing dependence of the TKE on the driving speed follows the findings of a previous study (Alonso-Estébanez et al., 2012). They concluded that the TKE generally increases with increasing driving speed for large vehicles, i.e. vans or trucks. For individual passenger cars, no significant increase in TKE was observed with increasing driving speed. The traffic data set used for the analysis in this thesis, which resolved the vehicle-types, did not include the driving speed. Therefore, with $\approx 90\%$ of the daily vehicle count being car-like vehicles in the Landshuter Allee (Table 5), the overall traffic in the Landshuter Allee is presumably more representative for the passenger cars.

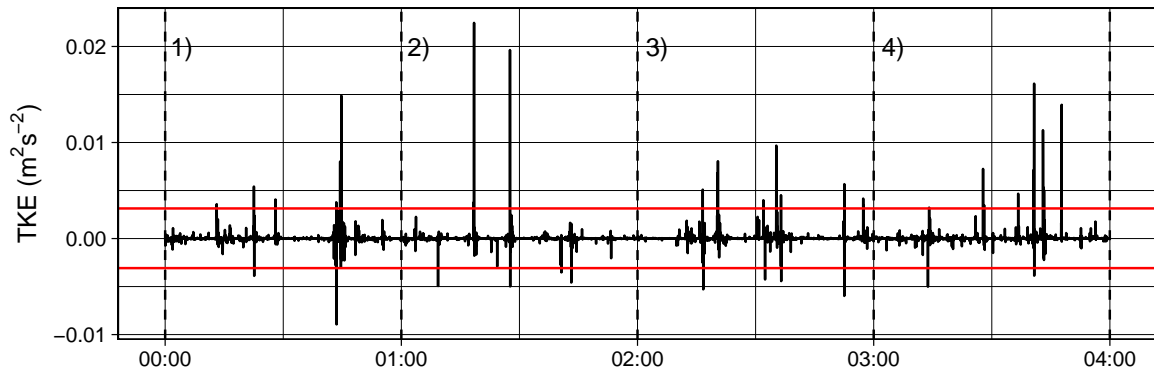


Figure 38.: Time series of the TKE for the time period from 00:00 to 4:00 for the night between the 20.07. and the 21.7. The temporal resolution is 1.5 s. The red lines indicate the mean TKE over the 4-hour period $\pm 5\sigma$

To investigate the presumption that large vehicles have a greater impact on the TKE than small vehicles, the raw EC-data of the streetside sonic anemometer was recalculated with a perturbation time scale of 1.5 s for one night. 1.5 s was chosen for τ because it is the approximate time it takes a truck to pass by the LÜB-station and nighttime conditions were chosen, because during nighttime the percentage of truck-like vehicles was larger and the overall number of vehicles lower. This simplifies and possibly enables the detection of individual vehicles. It is presumed that the spikes in the highly-resolved TKE correspond to the number of truck-like vehicles that passed by the sonic anemometer. For the comparison, the night between the 20.07. and the 21.7. was selected because of the consistently low TKE (Figure 31) and the north-wind dominated conditions (Figure 29). The TKE spiked several times per hour during the period from 00:00 to 4:00 (Figure 38). The hourly count of truck-like vehicles for the two driving lanes closest to the LÜB-station was in the same range of several per hours but not equal (Table 38). However, this indicates that the spikes in TKE could potentially be correlated with higher-resolution traffic data. Information on the vehicle count not per hour but per minute could provide temporally better correlated data and consequently enable a more precise spike-detection routine. In addition, the influence of the vehicles on the other driving lanes should not be neglected. Even though the influence of vehicles on the TKE decreases with increasing distance from the measuring instruments (Alonso-Estébanez et al., 2012), the vehicles on the driving lanes at a greater distance from the sonic anemometers might also affect the TKE.

Table 9.: Overview of the hourly number of truck-like vehicles in the time period from 00:00 to 4:00 for the night between the 20.07. and the 21.7., the hourly number of all vehicles, the corresponding percentage of truck-like vehicles per hour and the number of spikes detected in the TKE signal of the streetside sonic. All data points outside the range of the mean TKE $\pm 5\sigma$ were considered as spikes.

Interval	No. of spikes	No. of truck-like vehicles	total No. of vehicles	% of truck-like vehicles
00:00 - 1:00	5	6	54	11.1 %
01:00 - 2:00	5	6	18	33.3 %
02:00 - 3:00	7	4	25	16.0 %
03:00 - 4:00	6	4	19	21.1 %

3.3.2.3 Dependence of the friction velocity u_* on the mean wind speed \bar{u}

During the two-month measurement period, the wind speed \bar{u} was on average slightly higher on the weekdays compared to the weekends (Figure 39, left panel). Since the most common wind direction is aligned with the street orientation and the driving direction and there is significantly more traffic on the weekdays, the vehicles potentially have an enhancing influence on the wind speed. The presumed effect of moving vehicles on \bar{u} was observed at the DWD station. In the Helene-Weber-Allee, \bar{u} was on average the same for the weekend and the weekdays (Figure 39, right panel). However, the main prevailing wind directions in the Helene-Weber Allee did not align with the street orientation and the instruments are not installed as close to the traffic as the sonic anemometers at the LÜB-station.

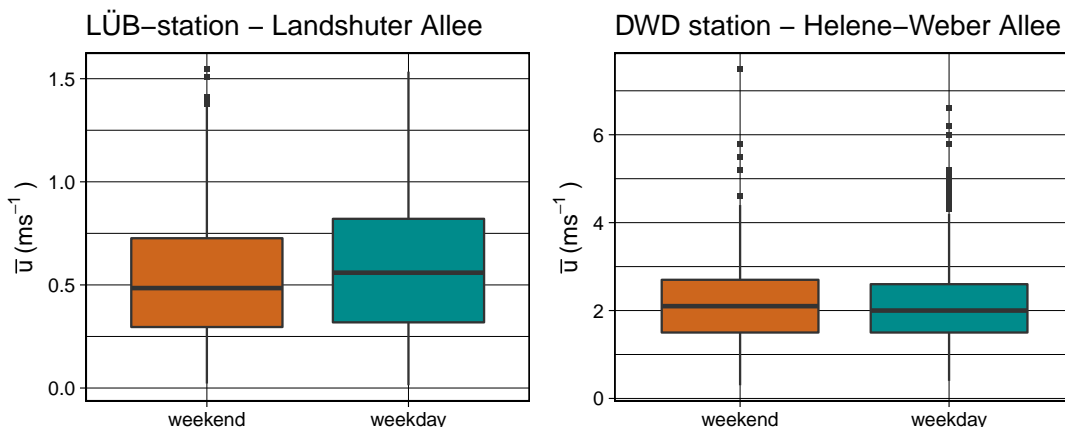


Figure 39.: Box plots illustrating the average wind speed \bar{u} for the two-month measurement period differentiated by weekend and weekday for the LÜB-station in the Landshuter Allee (left panel) and the DWD station in the Helene-Weber Allee (right panel).

The friction velocity u_* and the mean wind speed \bar{u} well correlated during the two-month measurement period (Figure 40). For low wind speeds, the relationship between u_* and \bar{u} was close to linear. However, above a wind speed of 0.5 ms^{-1} , u_* did not increase linearly with \bar{u} and as a consequence, the curve flattens. This trend was observed for the weekends as well as the weekdays.

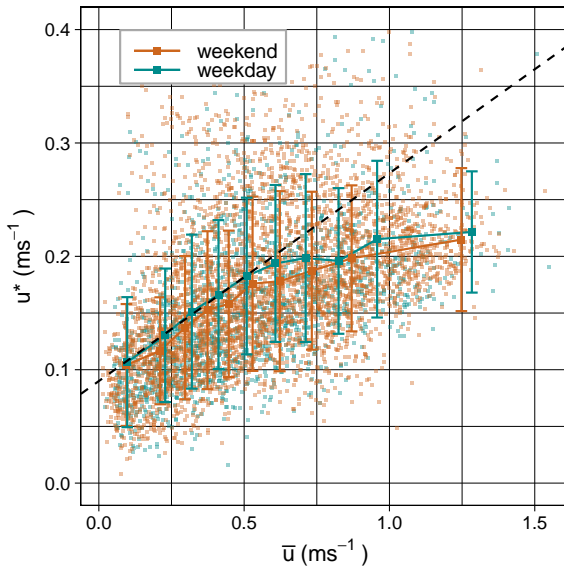


Figure 40: Dependency of the friction velocity u_* on the mean wind speed \bar{u} differentiated by weekend and weekday. The mean values of u_* correspond to dynamic bin values of \bar{u} . Each data point represents one half-hourly interval of the two-month measurement period. The error bars denote \pm one standard deviation.

It is commonly observed that u_* increases more rapidly with increasing wind speed above a threshold wind speed. For weak winds the slope is smaller compared to the slope for stronger wind speeds. For weak-wind regimes the dependence of u_* on the mean flow is only weak while above the threshold wind speed, the surface turbulence strongly depends on \bar{u} . This threshold wind speed is determined by the thermal characteristics of the surface, as well as the surface roughness and energy budget (Mahrt et al., 2014). In contrast to this usually observed correlation, in this study, the slope was larger for weaker winds. u_* strongly depended on the mean wind speed also for the smallest wind speeds, likely because there is always shear present in a street canyon with high surface roughness. u_* increased slower instead of stronger for increasing wind speeds. The smaller wind slope for the high wind speeds can potentially be explained by increasing saturation of the turbulence and decoupling of the turbulence surface due to the traffic.

4. Conclusions

In this thesis, turbulence measurements in the Landshuter Allee street canyon were investigated to gain a general understanding of turbulence regime in the street canyon and what influencing factors it depends on.

The results of this thesis show that the structure and the building morphology of the Landshuter Allee control the air flow and turbulence regime within the street canyon. The wind is mostly channeled along the north-south orientation of the street. The synoptic flow perpendicular to the street orientation, is partially washed down by the building fronts, accelerated and deflected back into the canyon with a 180° reversal of the wind direction: synoptic easterly flow leads to westerly winds in the street canyon and vice versa. The wind speeds in the Landshuter Allee are generally small. The wind is stronger closer to the street compared to the sidewalk and is the largest for northerly and northwesterly flow. The larger wind speeds on the streetside result in stronger turbulence. Overall, the wind speed correlates with the turbulence strength: an increase in \bar{u} led to stronger turbulence. This increase is more pronounced for the northwesterly and westerly flow compared to southerly and northerly flow, resulting in higher TKE values for the reversed flow compared to the channeled flow, for the same wind speed. This relationship demonstrates that the recirculation of the winds in the street canyon enhances the turbulence. The stronger increase of the TKE for easterly winds indicates, that the shear generation was not only influenced by the wind recirculation but also by the VIT. The buoyancy production was strongly influenced by the proximity to the heat-storing buildings. For very winds in the street canyon, the turbulence-generation was buoyancy-driven.

The thesis further demonstrates that the surface layer in the Landshuter Allee was generally unstably stratified during the measurement period. Even though the nocturnal atmosphere is typically stably stratified, this rarely occurred in the Landshuter Allee due to strong anthropogenic heat release and the high surface roughness of the urban struc-

tures. Stratification did therefore not suppress turbulent vertical mixing. Yet, the two-month observational period did not cover a full annual cycle and was consequently not influenced by seasonality. Neutral stability occurred slightly more often towards the end of the measurement period. This indicates a potentially more neutrally or stably stratified atmosphere in the fall and winter months. The presumed increase in episodes with neutral stratification is likely to result in increased mean wind speeds and consequently leads to stronger turbulence.

One of the main points of this thesis was the question about the influence of vehicle-induced turbulence. The comparatively stronger turbulence on weekdays and closer to the street, confirmed the assumption that the movement of vehicles enhances the turbulence. The positive correlation between the turbulence strength and the vehicle movement depended on the traffic intensity. Above a certain threshold value for the vehicle count, the amplification of turbulence by vehicle movement was counteracted by the blocking effect due to congested traffic. In the Landshuter Allee, this blocking effect was observed for the afternoon rush hour.

The results from this thesis provide the basis for understanding the main turbulence generating mechanisms in the Landshuter Alle. Turbulent motions are presumably the dominant process in pollution dispersion in the Landshuter Allee. Because the wind in the street canyon is generally weak, there is only little potential to produce turbulence. It seems that for the street-typical, channeled north wind, there is only low ventilation possible and the turbulence-suppressing effect of high traffic intensities likely further enhances the peak in air pollution concentrations during the rush hour. Only for the recirculation flow regime, more turbulence is produced and the greater vertical mixing potentially reduces the concentration of air pollutants.

Acknowledgements

First, I would like to express my gratitude to my primary supervisor, Prof. Dr. Christoph Thomas, who continuously supported me throughout this project. He always provided me with constructive criticism, valuable advice and insightful comments that guided me through the field experiment, the data analysis and interpretation. I wish to extend my gratitude to my secondary supervisor, Dr. Wolfgang Babel, who always found time to help me with technical issues and programming-related problems.

This thesis is a contribution to the the REINELUFFT? project which was funded by Bavarian State Ministry of the Environment, Public Health and Consumer Protection. I highly appreciate the assistance provided by the REINELUFFT? research team. I have greatly benefited from the lively scientific and interdisciplinary exchange and the many insightful suggestions. I am particularly grateful for the help of Frederik Bachman from the Technical University of Munich who provided me with the traffic datasets.

I would also like to thank all members of the Micrometeorology group for the helpful contributions and practical suggestions during our biweekly group meetings. Special thanks to Johann Schneider for his help on setting up and conducting the field experiment and to Leyla Sungur for patiently introducing me to the PALM model system even though this did not become part of my thesis in the end.

Literature

- Ahmad, K., Khare, M., and Chaudhry, K. (2005). "Wind tunnel simulation studies on dispersion at urban street canyons and intersections—a review". In: *Journal of Wind Engineering and Industrial Aerodynamics* 93.9, pp. 697–717. DOI: 10.1016/j.jweia.2005.04.002.
- Alonso-Estébanez, A., Pascual-Muñoz, P., Yagüe, C., Laina, R., and Castro-Fresno, D. (2012). "Field experimental study of traffic-induced turbulence on highways". In: *Atmospheric Environment* 61, pp. 189–196. DOI: 10.1016/j.atmosenv.2012.07.032.
- Aubinet, M., Vesala, T., and Papale, D., eds. (2012). *Eddy Covariance: A Practical Guide to Measurement and Data Analysis*. Vol. 12. Journal Abbreviation: Springer Atmospheric Sciences Series. Springer Atmospheric Sciences. 451 pp. DOI: 10.1007/978-94-007-2351-1.
- Battista, G., Evangelisti, L., Guattari, C., and Vollaro, R. D. L. (2015). "On the Influence of Geometrical Features and Wind Direction over an Urban Canyon Applying a FEM Analysis". In: *69th Conference of the Italian Thermal Engineering Association, ATI 2014* 81, pp. 11–21. DOI: 10.1016/j.egypro.2015.12.054.
- Bayerisches Landesamt für Umwelt, ed. (2021). *Langzeitverläufe der Schadstoffbelastung an den bayerischen LÜB-Messstationen: Stickstoffdioxid (NO₂)*.
- Boussinesq, J. (1877). "Essai sur la theorie des eaux courantes. Memoires presentes par divers savants a l'Academie des Sciences de l'Institut National de France, Tome XXIII". In: 1, pp. 1–680.
- Cai, C., Ming, T., Fang, W., Richter, R. de, and Peng, C. (2020). "The effect of turbulence induced by different kinds of moving vehicles in street canyons". In: *Sustainable Cities and Society* 54, p. 102015. DOI: 10.1016/j.scs.2020.102015.
- Di Sabatino, S., Kastner-Klein, P., Berkowicz, R., Britter, R., and Fedorovich, E. (2003). "The Modelling of Turbulence from Traffic in Urban Dispersion Models — Part I: Theoretical Considerations". In: *Environmental Fluid Mechanics* 3.2, pp. 129–143. DOI: 10.1023/A:1022063608237.
- Foken, T. (2017). *Micrometeorology*. 2nd ed. Springer-Verlag Berlin Heidelberg. 362 pp.
- Funk, D. (2014). *Stadtklimaanalyse Landeshauptstadt München*. Hannover: GEO-NET Umweltconsulting GmbH, p. 66.
- Järvi, L., Rannik, Ü., Kokkonen, T. V., Kurppa, M., Karppinen, A., Kouznetsov, R. D., Rantala, P., Vesala, T., and Wood, C. R. (2018). "Uncertainty of eddy covariance flux measurements over an urban area based on two towers". In: *Atmospheric Measurement Techniques* 11.10, pp. 5421–5438. DOI: 10.5194/amt-11-5421-2018.
- Kalthoff, N., Bäumer, D., Corsmeier, U., Kohler, M., and Vogel, B. (2005). "Vehicle-induced turbulence near a motorway". In: *The Karlsruhe Autobahn-Campaign BAB II: Validation of Emission Data* 39.31, pp. 5737–5749. DOI: 10.1016/j.atmosenv.2004.06.048.

- Karra, S., Malki-Epshtein, L., and Neophytou, M. K.-A. (2017). "Air flow and pollution in a real, heterogeneous urban street canyon: A field and laboratory study". In: *Atmospheric Environment* 165, pp. 370–384. DOI: 10.1016/j.atmosenv.2017.06.035.
- Kastner-Klein, P., Fedorovich, E., and Rotach, M. (2001). "A wind tunnel study of organised and turbulent air motions in urban street canyons". In: *Journal of Wind Engineering and Industrial Aerodynamics* 89.9, pp. 849–861. DOI: 10.1016/S0167-6105(01)00074-5.
- Klein, P. M. and Galvez, J. M. (2015). "Flow and turbulence characteristics in a suburban street canyon". In: *Environmental Fluid Mechanics* 15.2, pp. 419–438. DOI: 10.1007/s10652-014-9352-5.
- Lelieveld, J., Evans, J. S., Fnais, M., Giannadaki, D., and Pozzer, A. (2015). "The contribution of outdoor air pollution sources to premature mortality on a global scale". In: *Nature* 525.7569, pp. 367–371. DOI: 10.1038/nature15371.
- Li, X.-X., Britter, R., and Norford, L. K. (2016). "Effect of stable stratification on dispersion within urban street canyons: A large-eddy simulation". In: *Atmospheric Environment* 144, pp. 47–59. DOI: 10.1016/j.atmosenv.2016.08.069.
- Mahrt, L., Sun, J., and Stauffer, D. R. (2014). "Dependence of Turbulent Velocities on Wind Speed and Stratification". In: *Boundary-Layer Meteorology* 155, pp. 55–71.
- Makar, P. A., Stroud, C., Akingunola, A., Zhang, J., Ren, S., Cheung, P., and Zheng, Q. (2021). "Vehicle induced turbulence and atmospheric pollution". In: *Atmos. Chem. Phys. Discuss.* 2021. Publisher: Copernicus Publications, pp. 1–38. DOI: 10.5194/acp-2020-1243.
- Moore, C. J. (1986). "Frequency response corrections for eddy correlation systems". In: *Boundary-Layer Meteorology* 37.1, pp. 17–35. DOI: 10.1007/BF00122754.
- Pelliccioni, A., Monti, P., Gariazzo, C., and Leuzzi, G. (2012). "Some characteristics of the urban boundary layer above Rome, Italy, and applicability of Monin-Obukhov similarity". In: *Environmental Fluid Mechanics* 12, pp. 405–428.
- R Core Team (2021). *R: A Language and Environment for Statistical Computing*. R Foundation for Statistical Computing. Vienna, Austria.
- Ramer, S. (2021). "Untersuchung der Strömungsregime und deren Zusammenhang mit den Luftschadstoffkonzentrationen in einer Straßenschlucht mit hoher Verkehrsdichte in der Landeshauptstadt München". Bachelor Thesis. University of Bayreuth.
- Roth, M. (2000). "Review of atmospheric turbulence over cities". In: *Quarterly Journal of the Royal Meteorological Society* 126.564, pp. 941–990. DOI: 10.1002/qj.49712656409.
- Sarrat, C., Lemonsu, A., Masson, V., and Guedalia, D. (2006). "Impact of urban heat island on regional atmospheric pollution". In: *Atmospheric Environment* 40.10, pp. 1743–1758. DOI: <https://doi.org/10.1016/j.atmosenv.2005.11.037>.
- Sicard, P., Agathokleous, E., De Marco, A., Paoletti, E., and Calatayud, V. (2021). "Urban population exposure to air pollution in Europe over the last decades". In: *Environmental Sciences Europe* 33.1, p. 28. DOI: 10.1186/s12302-020-00450-2.
- Taylor, G. I. (1938). "The Spectrum of Turbulence". In: *Proceedings of the Royal Society of London. Series A - Mathematical and Physical Sciences* 164.919. Publisher: Royal Society, pp. 476–490. DOI: 10.1098/rspa.1938.0032.

-
- Thomas, C., Law, B., Irvine, J., Martin, J., Pettijohn, J., and Davis, K. (2009). "Seasonal hydrology explains interannual and seasonal variation in carbon and water exchange in a semi-arid mature ponderosa pine forest in Central Oregon". In: *Journal of Geophysical Research*. DOI: 10.1029/2009JG001010.
- Umweltbundesamt, ed. (2021). *Jahresbilanzen der aktuellen Luftdaten: 2021*.
- Vachon, G., Louka, P., Rosant, J.-M., Mestayer, P., and Sini, J.-F. (2002). "Measurements of Traffic-Induced Turbulence within a Street Canyon during the Nantes'99 Experiment". In: *Water, Air and Soil Pollution: Focus* 2.5, pp. 127–140. DOI: 10.1023/A:1021323031600.
- Vickers, D. and Mahrt, L. (1997). "Quality Control and Flux Sampling Problems for Tower and Aircraft Data". In: *Journal of Atmospheric and Oceanic Technology* 14.3. Place: Boston MA, USA Publisher: American Meteorological Society, pp. 512–526. DOI: 10.1175/1520-0426(1997)014<0512:QCAFSP>2.0.CO;2.
- Yousefian, S., pourjafar, M., Mahdavinejad, M., and Moshfeghi, M. (2021). "Assessing the effects of urban canyon's open space and CO dispersion with using CFD". In: *Journal of Environmental Studies* 47.3, pp. 239–258. DOI: 10.22059/jes.2021.327715.1008206.
- Zajic, D., Fernando, H., Calhoun, R., Princevac, M., Brown, M., and Pardzjak, E. (2011). "Flow and Turbulence in an Urban Canyon". In: *Journal of Applied Meteorology and Climatology* 50, pp. 203–223. DOI: 10.1175/2010JAMC2525.1.

A. Power- and co-spectra (Sonic 2)

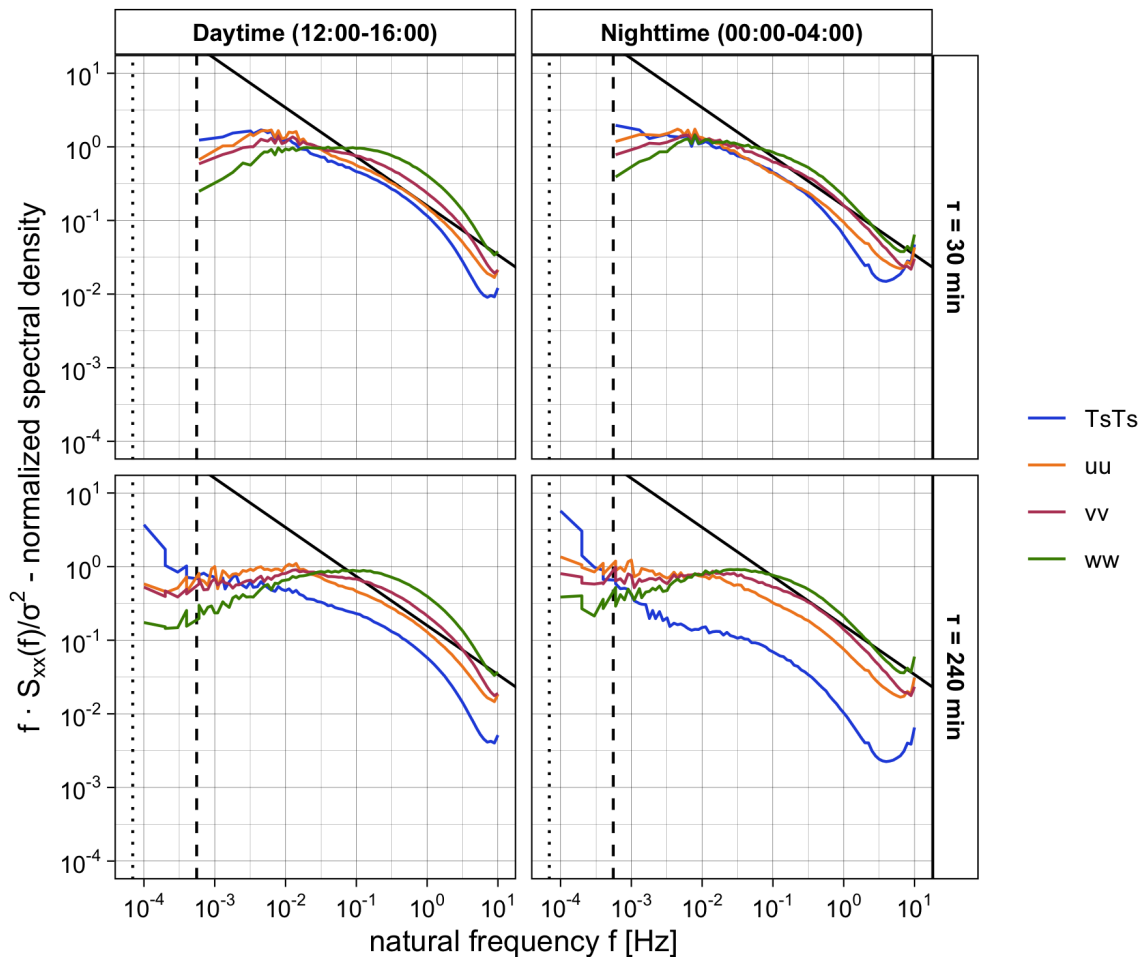


Figure 41.: Mean power-spectra (S_{xx}) for the variable x where x is the horizontal or vertical wind velocity or the sonic temperature T_S . The power-spectra were multiplied by the frequency f and normalized by the variance of x . The black solid lines indicates the $-2/3$ slope that is expected for the inertial subrange in the surface layer. The dashed vertical line corresponds to $\tau = 30$ min and the dotted vertical line to $\tau = 240$ min. The mean power-spectra was computed for the two-month observational period for the measurements of the streetside sonic anemometer and further subdivided by daytime (12:00-16:00) and nighttime (00:00 - 4:00).

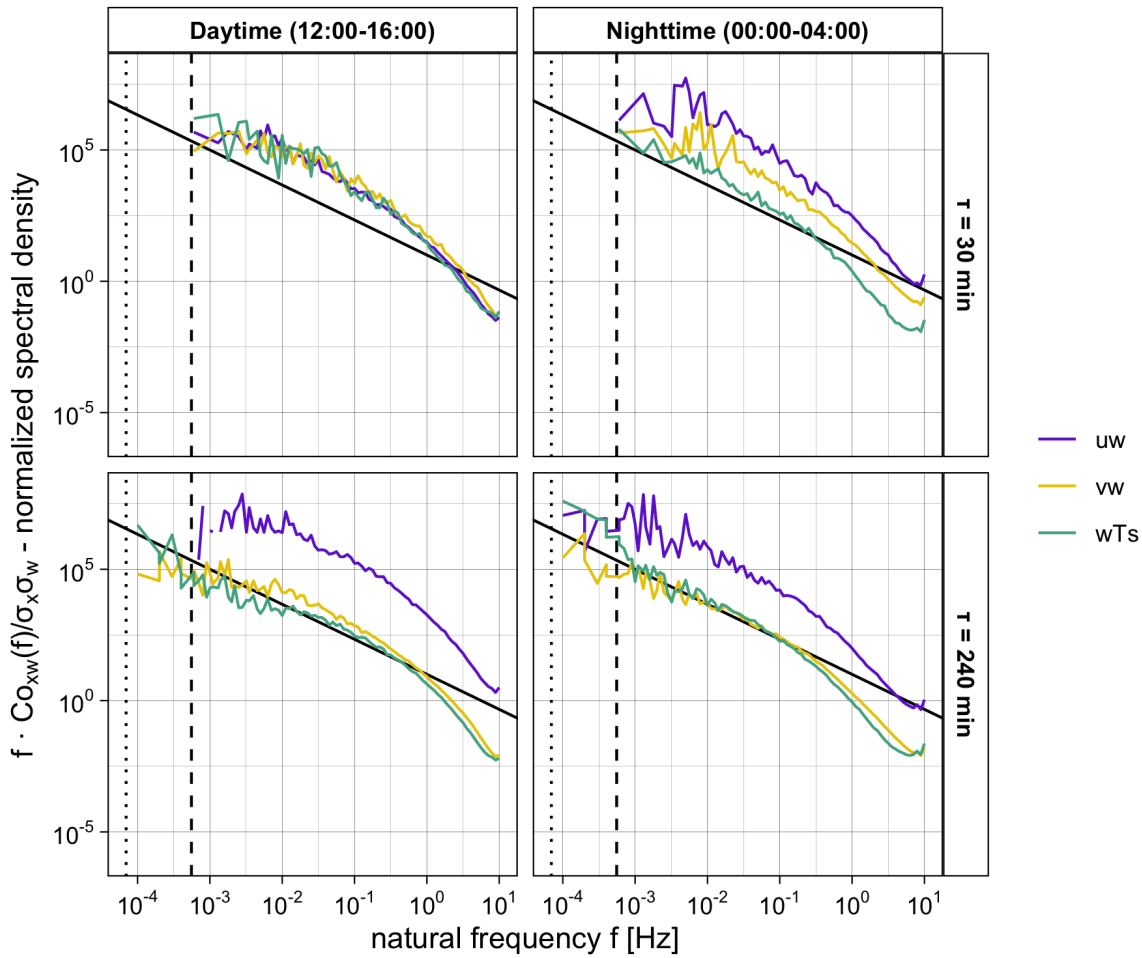


Figure 42.: Mean co-spectra ($Co_{x,w}$ between the vertical wind w and the variable x where x is the horizontal wind or the sonic temperature T_S). The co-spectra were multiplied by the frequency f and normalized by the covariance. The black solid lines indicates the $-4/3$ slope that is expected for the inertial subrange in the surface layer. The dashed vertical line corresponds to $\tau = 30$ min and the dotted vertical line to $\tau = 240$ min. The mean co-spectra was computed for the two-month observational period for the measurements of the streetside sonic anemometer and further subdivided by daytime (12:00-16:00) and nighttime (00:00 - 4:00).

Declaration of Authorship

Hereby, I declare that I have authored the master thesis titled

*"Air flow in a high-traffic urban street canyon: An experimental study
investigating turbulent transport in the Landshuter Allee in Munich, Germany."*

independently based on my own work. All direct or indirect sources used are acknowledged as references. This thesis has not been published or previously submitted to any other examination board. This work does not claim to be complete.

Bayreuth, 04.04.2022

Sophie Arzberger